

Lawrence Berkeley National Laboratory

LBL Publications

Title

Effect of hydrogen isotope on plasma impedance and thermal pinching induced by single aerosol droplets injected into an inductively coupled plasma

Permalink

<https://escholarship.org/uc/item/311149hf>

Authors

Chan, George C-Y
Hieftje, Gary M

Publication Date

2021-02-01

DOI

10.1016/j.sab.2020.106035

Peer reviewed

1
2
3
4
5
6
7
8
9
10
11
12
13
14
15
16
17
18
19
20
21
22
23
24
25
26
27
28
29
30
31
32
33
34
35
36
37
38
39
40
41
42
43
44
45
46
47
48
49
50
51
52
53
54
55
56
57
58
59
60
61
62
63
64
65

**Effect of hydrogen isotope
on plasma impedance and thermal pinching
induced by single aerosol droplets injected
into an inductively coupled plasma**

George C.-Y. Chan^{1,2*} and Gary M. Hieftje^{1*}

¹ Department of Chemistry, Indiana University, 800 E. Kirkwood Avenue, Bloomington, IN 47405, USA.

² Lawrence Berkeley National Laboratory, 1 Cyclotron Road, Berkeley, CA 94720, USA.

*corresponding authors, email: gcchan@lbl.gov (George Chan), hieftje@indiana.edu (Gary Hieftje)

1
2
3
4 **1 Abstract**
5
6
7

8 2 The mass of the hydrogen isotope in micrometer-sized aqueous droplets introduced into
9
10 3 an ICP has been found to affect the degree of resulting plasma perturbation. Studied
11
12 4 plasma perturbations include local plasma cooling, plasma shrinkage due to thermal
13
14 5 pinching, and changes in plasma impedance. The local cooling effect caused by a
15
16 6 vaporizing aerosol droplet was found to be similar between H₂O and D₂O. This finding
17
18 7 is likely a result of the similar heat capacities and vaporization rates of H₂O and D₂O
19
20 8 droplets and of the comparable thermal conductivities and dissociation kinetics of H₂O
21
22 9 and D₂O vapor. In contrast, a clear isotope effect was observed for plasma shrinkage and
23
24 10 impedance change, with H₂O causing a considerably stronger effect. Plasma shrinkage,
25
26 11 gauged by the reduction in Ar emission at the edge of the plasma, was detected at all
27
28 12 observation heights within the load-coil region, with D₂O droplets causing as much as
29
30 13 30% less of an effect than H₂O. Likewise, D₂O droplets induce significantly less change
31
32 14 in plasma impedance than H₂O droplets. Depending on experimental conditions and the
33
34 15 probing method, changes in plasma impedance caused by monodisperse D₂O droplets
35
36 16 were only 52%–80% that of H₂O. The lower influence on plasma shrinkage and
37
38 17 impedance change for D₂O droplets is believed to be related to the much lower thermal
39
40 18 conductivity of atomic deuterium, around 70% that of atomic hydrogen (protium). The
41
42 19 time required for the plasma impedance to return to its original steady-state value was
43
44 20 comparatively long (~10 ms) and similar for H₂O and D₂O droplets.
45
46
47
48
49
50
51
52
53
54
55

56 21 **Keywords:** inductively coupled plasma; aerosol perturbation; monodisperse droplets;
57
58 22 plasma pinch; plasma impedance; heavy water
59
60
61
62
63
64
65

1
2
3
4 24 **1. Introduction**
5
6
7

8 25 Although the inductively coupled plasma (ICP) is now regarded as a common workhorse
9
10 26 for elemental analysis and despite many outstanding mechanistic studies that have been
11
12 27 reported for processes occurring inside the plasma [1-5], there are still unsettled questions
13
14
15 28 [6, 7]. One such question involves the influence of an introduced aerosol on the
16
17 29 properties and behavior of the ICP. In addition, the burgeoning application of the ICP to
18
19
20 30 single-particle analysis [8, 9] requires a better understanding of the interplay among
21
22 31 introduced aerosol droplets and solute particles, the various plasma species, as well as
23
24
25 32 energy coupling and flow in the plasma. The introduction of monodisperse droplets into
26
27 33 an analytical flame [10, 11] or ICP [12-20], has long been recognized as a powerful
28
29
30 34 means for gaining new insights into fundamental signal-production processes but also
31
32 35 provides a useful tool to investigate these questions.
33
34
35

36 36 One particularly interesting question is what causes the observed change in plasma
37
38 37 impedance and shrinkage of plasma size (thermal pinching) when a single micrometer-
39
40 38 sized droplet is introduced into the ICP. We earlier reported a significant shift in plasma
41
42 39 impedance when single aerosol droplets of 27 μm (i.e., ~ 10 pL in volume) are sent into
43
44 40 the ICP [21]; others noted a shift in the radiofrequency delivered by a free-running
45
46 41 generator upon injection of a single droplet into the plasma [22]. More recently, through
47
48 42 the use of time-resolved two-dimensional monochromatic imaging, a sequence of plasma
49
50 43 perturbations involving local cooling, plasma reheating and thermal pinching during
51
52 44 single-droplet introduction was described [23]. The impedance change lasted a
53
54 45 comparatively long time (~ 10 ms). Four transition points, based on the derivative (i.e.,
55
56
57
58
59
60
61
62
63
64
65

1
2
3
4
5
6
7
8
9
10
11
12
13
14
15
16
17
18
19
20
21
22
23
24
25
26
27
28
29
30
31
32
33
34
35
36
37
38
39
40
41
42
43
44
45
46
47
48
49
50
51
52
53
54
55
56
57
58
59
60
61
62
63
64
65

46 rate of change) of the impedance-probe signal, were unambiguously identified and found
47 to correlate qualitatively with particular stages of plasma perturbation [23]. Specifically,
48 the first and last transition points were correlated with the moments when the plasma
49 shrinkage became established and started to ease, respectively [23]. It was hypothesized
50 that plasma shrinkage during droplet introduction was the result of a thermal pinch effect
51 caused by hydrogen liberated from the decomposition of volatilized water. Because the
52 thermal conductivity of atomic hydrogen is over one order of magnitude higher than that
53 of argon [24, 25], the increased thermal conductivity of the bulk plasma accelerates heat
54 loss at the plasma periphery. Consequently, the plasma shrinks in size in response to the
55 increased heat loss.

56 The objective of the present follow-up work is to test the aforementioned hypothesis and
57 to verify the role of liberated hydrogen when a single aerosol droplet is introduced into
58 the ICP. A straightforward way to address this question is to compare the effect of
59 hydrogen (protium) with its isotope – deuterium. Because of the very large fractional
60 difference between the atomic masses of hydrogen and deuterium and the well-known
61 relationship between thermal conductivity of a monatomic gas and reciprocal of the
62 square root of its atomic mass (i.e., $\text{mass}^{-1/2}$) [26-28], a large difference would be expected
63 between H₂O and D₂O droplets if the hypothesis is correct that atomic hydrogen is the
64 dominant cause of plasma shrinkage and plasma impedance change. Accordingly,
65 changes in plasma impedance and thermal pinching during injection of single aerosol
66 droplets in the form of H₂O and D₂O were measured and compared.

67 2. Experimental

68 The experimental setup (hardware) was identical to that previously described [23], with
69 modifications in experimental conditions and procedures as noted below. The system
70 consisted of an ICP generator, a set of entrance optics, a monochromatic imaging
71 spectrometer equipped with an intensified and gated charged-coupled device (ICCD)
72 detector, a commercial monodisperse microdroplet dispenser, an in-house-built trigger
73 circuit to signal droplet introduction into the plasma, and two separate devices for
74 measurement of any droplet-induced change in plasma impedance. A brief, yet self-
75 contained account of the experimental setup is given below; more detail can be found in
76 our previous publication [23].

77 2.1 Experimental setup

78 The ICP system and its operating conditions were common for this type of work [21, 23,
79 29]. The ICP generator (HFP-2500F, Plasma-Therm, Kresson, NJ, USA) was crystal-
80 controlled at 27.12 MHz and was operated at a forward power of 1200 W. The inner
81 diameter of the torch injector was 1.5 mm, and the torch was vertically mounted. The
82 commercial monodisperse microdroplet dispenser (MD-K-150-010, Microdrop GmbH,
83 Norderstedt, Germany) produced microdroplets with a nominal diameter of 50 μm (i.e.,
84 65 pL). The dispenser was mounted vertically and directly onto the base of the ICP torch
85 *via* a glass ball-joint adaptor, and introduced monodisperse droplets into the ICP at a
86 user-selectable rate set here at 33 Hz. The droplet stream was entrained by a flow of
87 argon and travelled vertically into the ICP. Three central-channel Ar flow rates of 0.155,
88 0.175 and 0.200 L/min were studied. These central-channel flows are much lower than

1
2
3
4 89 those in typical solution nebulization but are common for microdroplet injection without
5
6 90 a desolvator [30].
7
8
9

10 91 A 1-m focal-length Czerny-Turner spectrometer was configured as a monochromatic
11
12 92 imaging spectrometer [31, 32]. This arrangement provided two-dimensional
13
14
15 93 monochromatic images of the ICP at selected wavelengths. The spectral bandpass was
16
17
18 94 ~0.8 nm, adequate for the emission lines employed in this work. Each monochromatic
19
20 95 image of the plasma was captured by a gated ICCD with its pixels binned in groups of
21
22
23 96 4×4 to give a final 256×256 image [23]. Forty sequential ICCD images were taken, at
24
25 97 each studied wavelength, at increasing delay times in steps of 100 μs , referenced to a
26
27
28 98 droplet-introduction event. The gate widths for all ICCD images were held constant at
29
30 99 100 μs .
31
32
33

34 100 The trigger signal for the ICCD was supplied from a photomultiplier tube, with a narrow-
35
36
37 101 bandpass interference filter selective for the H_{α} emission line (center $\lambda = 656.4$ nm,
38
39 102 $\Delta\lambda = 1$ nm, 656FS02-25, Andover Corp., Salem, NH, USA) placed in front of the
40
41
42 103 photocathode window. Because of its construction, this signal is termed H_{α} -PMT,
43
44
45 104 independent of the emission from the actual hydrogen isotopes (i.e., H or D) that was
46
47 105 measured. This emission was collected between the lowest and middle turns of the load
48
49
50 106 coil. The trigger signal actually fires several hundred microseconds before the intact
51
52 107 droplet enters into the plasma because solvent evaporation starts when the droplet leaves
53
54
55 108 the capillary of the droplet dispenser, and water vapor accelerates faster thus reaches the
56
57 109 plasma earlier than the droplet.
58
59
60
61
62
63
64
65

1
2
3
4 110 Two methods, both indirect, were used to gauge plasma impedance. The first was
5
6 111 through the voltage induced in a RF-probe coil placed inside the plasma-torch
7
8
9 112 compartment. The second means was through the signal from the phase detector of the
10
11 113 impedance-matching network of the ICP instrument. Signals from the RF-probe coil, the
12
13
14 114 phase detector, and the H α -PMT (i.e., the trigger) were simultaneously measured and
15
16 115 digitized by a multi-channel digital oscilloscope and saved for further processing.
17
18
19
20

21 116 **2.2 Experimental procedures and data processing**

22
23
24 117 Two samples were used in this work – deionized water and heavy water (deuterium oxide,
25
26 118 99 atom %D, Sigma-Aldrich, St. Louis, Missouri, USA). A spike of barium standard,
27
28
29 119 from a stock solution at a concentration of 100 mg/L prepared in 2% HNO₃ (ordinary
30
31 120 water), was doped into both the deionized and heavy-water samples to give a final
32
33
34 121 concentration of 2 mg/L Ba in each. For brevity, these two samples are referred to as
35
36 122 H₂O and D₂O in this study.
37
38
39

40 123 In one experiment involving separate introduction of H₂O and D₂O droplets, a set of three
41
42 124 images were obtained at wavelengths corresponding to emission of the Ba analyte (Ba II
43
44
45 125 at 455.4 nm), hydrogen (H I at 656.3 nm or D I at 656.1 nm), and argon (Ar I at
46
47 126 696.5 nm). The integrated exposure time for each ICCD image was 5 s (i.e., introduction
48
49
50 127 of 165 single droplets). Steady-state plasma background emission was corrected by
51
52 128 subtraction of an ICCD image taken with the same settings, but at a delay time of 25 ms,
53
54
55 129 well after any perturbation caused by a droplet event has dissipated.
56
57
58
59
60
61
62
63
64
65

1
2
3
4
5
6
7
8
9
10
11
12
13
14
15
16
17
18
19
20
21
22
23
24
25
26
27
28
29
30
31
32
33
34
35
36
37
38
39
40
41
42
43
44
45
46
47
48
49
50
51
52
53
54
55
56
57
58
59
60
61
62
63
64
65

130 **3. Results and Discussion**

131 **3.1 The effect of hydrogen isotope on plasma impedance during single-droplet**
132 **introduction**

133 Figure 1 shows the temporal behavior of signals from the H_{α} -PMT, the RF-probe coil and
134 the phase-detector during repetitive introduction of single droplets into the ICP. The
135 displayed temporal profiles are the averages of five oscilloscope traces, each comprising
136 the averaged responses from 1280 single-droplet introduction events. As in our previous
137 studies [21, 23], the RF-probe coil and phase-detector signals were measured in ac-
138 coupling and dc-coupling modes, respectively. For both isotopic forms of hydrogen –
139 protium and deuterium – in the introduced droplets, large excursions in plasma
140 impedance occurred, as reflected in the significant changes in RF-probe coil and phase-
141 detector signals. However, D_2O droplets induced a clearly smaller change in plasma
142 impedance than H_2O . Quantitatively, the peak height in the change of the RF-probe coil
143 signal for D_2O droplets was about 64% of that for H_2O . Likewise, the dip in the phase
144 detector signal for D_2O was about 80% of that for H_2O .

145 It is, of course, essential to determine that this difference is not due to an artifact. We
146 earlier found [21] that both the RF-probe coil and phase-detector signal peaks are lower
147 for smaller droplets. Accordingly, it is important to confirm that the D_2O and H_2O
148 droplets are the same size when they reach the base of the plasma. For this evaluation, it
149 is tempting to use the H_{α} -PMT signal as a measure of droplet size; indeed, a quantitative
150 relationship between the two was assumed in our previous study [21]. However, this
151 proportionality might not hold for a comparison of H_2O and D_2O droplets because of a

1
2
3
4 152 difference in transmission efficiency of the interference filter employed in the H α -PMT
5
6
7 153 detection channel. First, the spectral bandpass of the H α interference filter is 1 nm, and
8
9
10 154 the isotopic shift between the H α (656.283 nm [33]) and D α (656.093 nm [33]) lines is
11
12 155 0.19 nm. Although the half width of the heavily Stark-broadened H α line is still only
13
14
15 156 around 0.1 to 0.2 nm [34], it is likely that not all of the H α spectral profile can pass
16
17 157 through the H α filter and also that the filter has dissimilar efficiencies for transmitting the
18
19
20 158 H α and D α emission lines. Second, for an interference filter to function properly, the
21
22 159 incoming beam needs to be collimated and to fall at normal incidence onto the filter
23
24
25 160 surface. If the incoming beam impinges at an angle onto the filter (i.e., tilted), the central
26
27 161 bandpass of the interference filter shifts to shorter wavelengths [35]. Because the original
28
29
30 162 intended purpose of the H α -PMT signal was to generate a trigger signal, no collimating
31
32 163 optics was used in light collection. Instead, as previously outlined [21, 29], the collected
33
34
35 164 plasma emission was only partially collimated by passing it through a ~ 20 cm black-
36
37 165 painted glass tube with an internal diameter of 3 mm. As a result, it is plausible that our
38
39
40 166 H α filter–PMT assembly favors the D α line, which emits at a shorter wavelength [33].
41
42 167 Furthermore, the ion-dynamic effect is not the same for H and D because of the
43
44
45 168 substantial difference in reduced mass of the radiator (H or D)–perturber (presumably Ar⁺)
46
47 169 system [36, 37]. As such, Stark profiles for H and D are also different. Compared to H α ,
48
49
50 170 reductions in Stark width (and hence increases in peak height) between 10% and 15% for
51
52 171 D α have been experimentally reported [36, 38, 39] and calculated [36, 38, 40] for electron
53
54
55 172 densities and temperatures typical of an analytical ICP. Thus, although we consistently
56
57 173 observed stronger PMT signals from the D₂O samples, we are reluctant to interpret the
58
59
60 174 H α and D α signals quantitatively.
61
62
63
64
65

1
2
3
4 175 Because it is experimentally difficult to measure the size of droplets immediately before
5
6 176 they enter the plasma, we offer two arguments that D₂O droplets are *not* smaller than
7
8
9 177 their H₂O counterparts. The first argument is based on literature results involving droplet
10
11 178 production and evaporation, and the second is from acquired ICCD images to be
12
13
14 179 presented in the next section. The outcome is that the observed smaller change in plasma
15
16 180 impedance for D₂O droplets is real and not due to smaller droplet sizes.
17
18

19
20 181 In the literature, Lazar and Farnsworth [17] evaluated the influence of the physical
21
22 182 properties of liquids on droplet production by a pizeoelectric-based micropump similar to
23
24 183 the one used in the present study. Their (and our) micropump employs a glass tube with
25
26
27 184 a restriction at the inlet and surrounded by a pizeoceramic sleeve [12, 17]. When the
28
29 185 pizeoceramic is energized, a compression pulse squeezes the glass tube and expels a
30
31 186 droplet [17]. The restriction at the tube inlet reduces the backflow of liquid and
32
33
34 187 strengthens droplet ejection at the exit. The viscosity of the liquid governs the amount of
35
36 188 backflow through the restriction during the compressive pulse [17]; the lower the
37
38 189 viscosity, the greater the backflow, and the smaller the droplet size at the tip of the
39
40 190 micropump [17]. Lazar and Farnsworth [17] found a linear correlation between the
41
42 191 droplet volume and viscosity of water, methanol and xylene. Accordingly, the
43
44 192 volumetric ratio of D₂O to H₂O at the exit of our droplet dispenser can be estimated from
45
46
47 193 the corresponding ratio of the viscosities. The viscosities of D₂O and H₂O are 1.247 [41]
48
49 194 and 1.002 [42] mPa s at 20°C (i.e., a ratio of 1.24) and are 0.972 [41] and
50
51 195 0.797 [42] mPa s, respectively, at 30°C (i.e., a ratio of 1.22). Therefore, according to the
52
53 196 viscosity argument, D₂O droplets are expected to be about 20% *larger* in volume (or 7%
54
55
56
57
58
59
60
61
62
63
64
65

1
2
3
4 197 larger in diameter) than H₂O droplets. This difference is opposite from what would be
5
6 198 necessary for the observed effect on plasma impedance.
7
8
9

10
11 199 Even if the D₂O and H₂O droplets are initially of identical size, they might evaporate at
12
13 200 dissimilar rates. Only if the evaporation rate of D₂O is not higher than that of H₂O can
14
15 201 we persuasively argue that D₂O droplets are *not* smaller than those of H₂O when they
16
17
18 202 enter the plasma. The boiling point of D₂O is 101.4°C, slightly higher than that of H₂O.
19
20
21 203 From room temperature to their boiling points, the vapor pressure of H₂O is always
22
23 204 slightly higher than D₂O, by an amount between 17% (at room temperature) and 6% (at
24
25 205 the boiling point) [43]. From the viewpoint of vapor pressure, it is *not* expected that D₂O
26
27
28 206 droplets evaporate faster than H₂O droplets during their journey from the dispenser to the
29
30
31 207 plasma; nor, therefore, are D₂O droplets likely to be smaller than those of H₂O.
32

33
34 208 Of course, droplet evaporation inside the ICP injector is likely not in vaporization
35
36 209 equilibrium, so evaporation kinetics need to be considered. The evaporation rates of
37
38
39 210 H₂O and D₂O droplets with diameters of 12 to 15 μm at temperatures between 3.6°C and
40
41
42 211 50.7°C injected into vacuum have been experimentally determined and were reported to
43
44 212 be nearly identical [44]. This finding agrees with a theoretical model based on competing
45
46
47 213 energetic and entropic effects [44]. Therefore, from arguments in the literature, we can
48
49
50 214 be confident that D₂O droplets are *not* smaller than those of H₂O when they enter the
51
52 215 plasma. An experimental inference is presented in the next section.
53
54
55
56
57
58
59
60
61
62
63
64
65

1
2
3
4 216 **3.2 Monochromatic emission images of H and Ba showing height of complete**
5
6 217 **droplet evaporation and initial solute-particle atomization**
7
8
9

10 218 Representative monochromatic emission images show that the heights of complete
11
12 219 vaporization of droplets from H₂O and D₂O are essentially identical, with a temporal
13
14
15 220 difference less than the exposure time of a single ICCD image frame (i.e., 100 μs).
16
17 221 Furthermore, through doping the droplets with Ba, it was found that the time for the first
18
19
20 222 appearance of Ba emission as well as the integrated Ba emission for H₂O and D₂O
21
22 223 droplets was indistinguishable. In all cases, the measured difference is not significant
23
24
25 224 compared to experimental uncertainties. If anything, evaporation of D₂O droplets is
26
27 225 marginally slower than H₂O droplets, suggesting that the D₂O droplets might be
28
29
30 226 marginally larger in size than those of H₂O.

31
32
33
34 227 Figure 2a shows the net (i.e., after background correction with an image taken at steady
35
36 228 state) monochromatic images, with a time stamp of 1.55 ms after the H_α-PMT trigger,
37
38
39 229 during single-droplet introduction into the plasma at H_α 656.3 nm and D_α 656.1 nm. The
40
41 230 exposure time of the ICCD was 100 μs, starting from 1.50 ms to 1.60 ms with respect to
42
43
44 231 the trigger. The scales marked on the *x*- and *y*-axes of the images represent the physical
45
46 232 size of the plasma. As detailed in several previous publications [23, 45, 46], because of
47
48
49 233 an optical artifact in the monochromatic imaging spectrometer, the vertical and horizontal
50
51 234 scales of the images are not identical but are correctable. Because a vaporizing droplet
52
53
54 235 serves as a local reservoir supplying hydrogen or deuterium atoms, the localized emission
55
56 236 in the image center (i.e., the red dot) pinpoints the location of the vaporizing droplet.
57
58
59 237 Also, as has been reported previously [23, 30], atomic hydrogen quickly diffuses
60
61
62
63
64
65

1
2
3
4 238 throughout the whole plasma. The positions of the hydrogen and deuterium atomic
5
6 239 clouds were at similar locations in the plasma – just above the second turn of the load coil,
7
8
9 240 counting from the bottom. A comparison of the two images reveals that the localized D_{α}
10
11 241 emission is stronger than that of H_{α} , suggesting that it took slightly longer for the D_2O
12
13 242 droplet to complete its evaporation in the plasma. In fact, the displayed H_{α} image is the
14
15 243 last one in the series in which a localized hydrogen emission cloud could be distinctly
16
17 244 identified. In the subsequent ICCD image frame, with a time stamp of 1.65 ms (cf.
18
19 245 Figure 2b), no localized H_{α} emission could be seen although localized D_{α} emission was
20
21 246 still present.
22
23
24
25
26
27

28 247 Figure 3 displays net monochromatic images of Ba II 455.4 nm emission 1.65 ms after
29
30 248 the H_{α} trigger during H_2O and D_2O droplet introduction. This is the first frame in which
31
32 249 a distinct Ba emission cloud could be observed for either H_2O or D_2O ; the images taken
33
34 250 at 1.55 ms (i.e., same time stamp as in Figure 2a, not shown) revealed no Ba emission.
35
36 251 Thus, although the last identifiable H_{α} and D_{α} emission clouds appeared respectively at
37
38 252 1.55 and 1.65 ms, the time lag between complete droplet evaporation for the H_2O and
39
40 253 D_2O was likely less than 100 μs , since the first appearance of analyte emission was at
41
42 254 1.65 ms in both cases. The fact that D_{α} emission (cf. Figure 2b) and Ba II emission
43
44 255 clouds appeared simultaneously in the same ICCD frame with a gate width of only
45
46 256 100 μs clearly argues that the processes of analyte atomization, ionization and excitation
47
48 257 after complete solvent evaporation are very fast, in agreement with a previous report [14].
49
50
51
52
53
54
55
56
57 258 From the vertical time-dependent centroid of the H_{α} and D_{α} emission clouds, one can
58
59 259 readily follow the acceleration of the H_2O and D_2O droplets in the plasma (cf. Figure 4).
60
61
62
63
64
65

1
2
3
4
5
6
7
8
9
10
11
12
13
14
15
16
17
18
19
20
21
22
23
24
25
26
27
28
29
30
31
32
33
34
35
36
37
38
39
40
41
42
43
44
45
46
47
48
49
50
51
52
53
54
55
56
57
58
59
60
61
62
63
64
65

260 This acceleration can be well represented by a quadratic function. The behavior in
261 Figure 4 is phenomenologically similar to that found in a chemical flame. Russo and
262 Hieftje [47] introduced monodisperse droplets of 68 μm diameter side-on into a chemical
263 flame and measured the vertical distance of the droplet in the flame as a function of its
264 residence time. Although a model of higher order (fourth order polynomial) was used
265 [47], the vertical height of the droplet in the flame can be adequately approximated with a
266 quadratic function. The bands in Figure 4 designated by horizontal dotted lines from -1.2
267 to -2.2 mm, from -7.5 to -8.5 mm, and from -13.8 to -14.8 mm denote three vertical
268 locations that will be discussed in detail in Section 3.4.

269 Spatial integration of emission from the Ba ion cloud (cf. Figure 3) could provide
270 additional insight into the relative sizes of the H_2O and D_2O droplets. To a first
271 approximation, if one assumes that the excitation environment is identical between H_2O
272 and D_2O droplet injection, the Ba emission will be directly proportional to the analyte
273 mass, which in turn is directly proportional to the initial droplet volume. Figure 5
274 displays the spatially integrated Ba emission with a window that runs laterally
275 between -2 mm and +2 mm of the plasma center and vertically from -9.73 mm to
276 +0.70 mm (i.e., all heights above the middle load coil, cf. Figure 3) at different delay
277 times. The small dip at ~ 1.4 ms before the appearance of the Ba emission spike is due to
278 local plasma cooling from the vaporizing droplet, causing a momentary drop in the
279 plasma continuum emission. The dip at ~ 1.9 ms is caused by part of the Ba emission
280 cloud being obscured by the load coil. Although the two Ba temporal profiles do not
281 overlap exactly, they are very close in shape and amplitude. In fact, if one further
282 integrates the temporal emission from 16 to 24 ms (i.e., from the time when Ba emission

1
2
3
4 283 started to when the Ba ion cloud moved out of the captured-image range), the difference
5
6 284 in the Ba emission between H₂O and D₂O droplets is smaller than the baseline noise (i.e.,
7
8
9 285 statistically insignificant).

10
11
12
13 286 Based on the experimental results discussed above, we are confident that the introduced
14
15 287 H₂O and D₂O droplets are very similar in size, and if there is a marginal difference, the
16
17
18 288 D₂O droplets could be slightly larger, but definitely *not* smaller than their H₂O
19
20 289 counterparts. This finding is critical, because as will be shown, plasma perturbations
21
22
23 290 induced by D₂O droplets are decidedly smaller than those by H₂O droplets.

24 25 26 27 291 **3.3 Monochromatic emission images of Ar showing plasma shrinkage**

28
29
30 292 Figure 6a shows the net absolute change in Ar I 696.5 nm emission during single-droplet
31
32
33 293 introduction. The time stamp for Figure 6a is 1.55 ms after the H_α-PMT trigger (same as
34
35 294 in Figure 2a). In this case, the droplet-induced change in Ar emission appears similar for
36
37
38 295 H₂O and D₂O. The most dramatic observation is the local cooling effect generated by the
39
40 296 droplets, which causes a substantial drop in argon emission in the center of the images.
41
42
43 297 In addition, H₂O and D₂O droplets both produce a sharp decline in Ar emission along the
44
45 298 two sides of the plasma. This plasma shrinkage is believed to be the result of thermal
46
47
48 299 pinching [48] due to a difference in thermal conductivity between the plasma gas (argon)
49
50 300 and the introduced foreign gas (in this case, the H₂O and D₂O droplets and/or their
51
52 301 dissociation products). The thermal pinching is not symmetrical, with a more prominent
53
54
55 302 effect found on the left side of the plasma images. As noted in our previous report [23],
56
57 303 the helical-shaped load coil likely causes the plasma asymmetry, especially within the
58
59
60
61
62
63
64
65

1
2
3
4 304 load-coil region. In addition, the curvature of the plasma torch tubing could induce
5
6 305 optical distortion in the collected plasma image, especially along the two sides [23].
7
8
9

10 306 Although the net change in Ar emission for H₂O and D₂O droplets appears similar in
11
12 307 Figure 6a, a considerable difference can be noted if the change is expressed as a
13
14 308 percentage (cf. Figure 6b). Here, percentage change in emission refers to the net change
15
16 309 (i.e., after subtraction of steady-state emission) relative to the steady-state emission. The
17
18 310 local cooling effect (i.e., the decrease in Ar emission close to the center of the image) is
19
20 311 similar for H₂O and D₂O whereas H₂O was found to induce a noticeably stronger plasma
21
22 312 pinching effect than D₂O; the percentage reduction in Ar emission, in particular on the
23
24 313 left edge of the plasma, is larger for H₂O. If one defines a threshold of 10% drop in Ar
25
26 314 emission to assess the degree of plasma shrinkage, the estimated size reduction was
27
28 315 2.3 mm and 1.8 mm, respectively, on the left side of the plasma for the introduction of
29
30 316 H₂O and D₂O droplets. The corresponding size decreases on the right side of the plasma
31
32 317 were 1.5 mm and 1.1 mm for H₂O and D₂O, respectively.
33
34
35
36
37
38
39
40

41 318 **3.4 Temporo-spatial change in Ar emission during single-droplet introduction**

42
43
44

45 319 In this section, the temporo-spatial change in relative argon emission upon H₂O and D₂O
46
47 320 droplet introduction will be compared. As already depicted in Figure 6b, two regions of
48
49 321 the plasma, its center and edge, are particularly affected by the droplets. Accordingly, the
50
51 322 average change in Ar emission within a radius of 0.9 mm of the plasma center and also in
52
53 323 a region within 0.8 mm from the left-hand edge of the plasma was calculated at three
54
55 324 vertical ± 0.5 mm-high windows, centered at -14.3, -8.0, and -1.7 mm with reference to
56
57 325 the top of the load coil.
58
59
60
61
62
63
64
65

1
2
3
4 326 Figure 7a shows the droplet-induced fractional change in Ar emission close to the bottom
5
6 327 of the load coil at a vertical height of -14.3 mm with reference to the top of the load coil.
7
8
9 328 In the center of the plasma, a similar change in Ar emission was observed for H₂O and
10
11 329 D₂O droplets, indicating that the local cooling effect caused by the droplet is independent
12
13
14 330 of the identity of the hydrogen isotope. There was a slight delay between the time when
15
16 331 the droplets were present within the observation volume and the moment when the
17
18
19 332 greatest Ar depression occurred. As noted in Figure 4, the droplet velocity was
20
21 333 comparatively low in the bottom part of the load coil and the droplet virtually stayed at
22
23
24 334 this observation height from about 0.45 to 0.65 ms whereas the maximum dip in Ar
25
26 335 emission occurred later, from 0.65 to 0.95 ms. At the left edge of the plasma, a more
27
28
29 336 pronounced depression in Ar emission was found, induced by plasma shrinkage. The
30
31 337 maximum percentage drop in Ar emission was ~12% at the edge, compared to ~7% in the
32
33
34 338 plasma center. Furthermore, the plasma shrinkage, as reflected by the percentage drop in
35
36 339 Ar emission at the edge, is sensitive to the isotopic form of hydrogen in the droplets. A
37
38 340 lesser effect, roughly by a factor of one-third, was observed with the D₂O droplets.
39
40
41 341 Moreover, the maximum plasma shrinkage happened around 1.0 to 1.5 ms, a time by
42
43 342 which the droplet had already moved quite far above the observation height (cf. Figure 4).
44
45
46 343 The cause for this significant delay was not determined, but could be due to the finite
47
48 344 transport time of the species (presumably atomic hydrogen or deuterium) responsible for
49
50
51 345 the plasma shrinkage, likely through recirculation, from the plasma center to its periphery.
52
53
54 346 The percentage change in Ar emission in the middle of the load-coil region (-8.0 mm) is
55
56 347 illustrated in Figure 7b. Similar to the case at -14.3 mm (cf. Figure 7a), H₂O and D₂O
57
58
59 348 droplets induced the same extent of local cooling in the plasma center. In addition, the

1
2
3
4 349 percentage drop in Ar emission in the plasma center is very comparable at the two
5
6 350 heights (~7 to 8%), despite the fact that the droplet is certainly becoming smaller during
7
8
9 351 its upward passage in the ICP. Similar unexpected observations have been reported
10
11 352 elsewhere [23]. It took roughly ~1.6 ms, with reference to the H α trigger (cf. Figure 4),
12
13
14 353 for the droplets to reach this vertical region of the plasma, which coincides with the time
15
16 354 of the maximum dip in Ar emission in the plasma center (cf. Figure 7b). At the edge of
17
18
19 355 the plasma, the hydrogen isotope effect again is apparent, with the influence of D $_2$ O
20
21 356 droplets significantly weaker than that of the H $_2$ O droplets. The maximum decrease in
22
23
24 357 Ar emission at the edge is ~16%, larger than the ~12% decrease at -14.3 mm.

25
26
27 358 Figure 7c shows the change in Ar emission even higher, in the upper part of the load-coil
28
29 359 region at an observation height centered at -1.7 mm. In the center of the plasma, here as
30
31 360 at other heights, the decline in Ar emission is similar for H $_2$ O and D $_2$ O droplets.
32
33 361 However, compared to lower positions (cf. Figures 7a and 7b) in which the drops in Ar
34
35 362 emission are about 7 to 8%, the dips here are only about 5%. The reduced effect is likely
36
37 363 because the droplets are completely vaporized at this vertical height (cf. Figure 4), so any
38
39 364 cooling effect is no longer created locally but is carried from upstream locations (lower
40
41 365 positions in the plasma) by the argon gas flow and is therefore diluted. The greatest dips
42
43 366 were at 1.55 ms and 1.95 ms, respectively, for observations at -8.0 mm and -1.7 mm,
44
45 367 giving an averaged velocity of about 16 m/s, which is about right for the linear gas
46
47 368 velocity in the upper part of the load-coil region [49, 50]. As reflected by the change in
48
49 369 Ar emission at the edge of the plasma, the plasma shrinkage effect continues to climb
50
51 370 from the bottom to the top of the load coil. Even at 0.6 ms, when the droplets are still
52
53 371 within the bottom part of the load coil (cf. Figure 4), plasma shrinkage at higher locations
54
55
56
57
58
59
60
61
62
63
64
65

1
2
3
4 372 could unambiguously be detected, suggesting rapid diffusion of the effect throughout the
5
6 373 plasma. Generally speaking, whenever plasma shrinkage is clearly detected, the effect
7
8
9 374 induced by H₂O droplets is larger than that by D₂O droplets, although the difference was
10
11 375 smaller compared to the behavior in lower regions of the load coil (cf. Figures 7a and 7b).
12
13
14

15 376 **3.5 Rate of change of plasma impedance**

16
17
18
19 377 Sections 3.1 and 3.4 compared changes in plasma impedance and plasma shrinkage that
20
21 378 resulted when monodisperse H₂O and D₂O droplets were introduced into the plasma. The
22
23
24 379 present section examines the rate of change in plasma impedance, which better reflects
25
26 380 the kinetics of whatever process causes the changes. Figure 8a displays the rate of
27
28
29 381 change (first derivative) of the RF-probe and phase-detector signals (collectively termed
30
31 382 plasma-impedance signals) as a function of time upon H₂O and D₂O droplet introduction.
32
33
34 383 Because the absolute changes in plasma impedance signals are smaller for D₂O droplets,
35
36 384 the rate of change for D₂O is also lower. In addition, slight delays were observed
37
38
39 385 between the temporal profiles of H₂O and D₂O. For instance, the minimum in the first
40
41 386 derivative for the phase-detector signal occurred at 0.63 and 0.83 ms, respectively, for
42
43 387 H₂O and D₂O. Likewise, the phase-detector signals reached their respective minimum
44
45 388 (i.e., when derivatives equal zero) at 1.61 ms for H₂O and 1.75 ms for D₂O. The RF-
46
47
48 389 probe signals exhibited slightly longer delays due to the slower circuit response [21, 23],
49
50
51 390 but yielded the same conclusion. Because the phase-detector circuit offered wider
52
53 391 bandwidth and hence better temporal accuracy and resolution, the phase-detector signal
54
55
56 392 was used as the primary reference to pinpoint the temporal change in plasma impedance.
57
58
59
60
61
62
63
64
65

1
2
3
4 393 The bandwidths of the RF-probe coil and phase-detector circuits were previously
5
6 394 determined to be 1,300 and 15,000 Hz, respectively [21].
7
8
9

10 395 Apart from the slight delay between the responses for H₂O and D₂O (i.e., slight
11
12 396 horizontal shift in the time axis), the overall shapes of the temporal profiles for the rate of
13
14 397 change are similar, which is even more apparent if the temporal profiles of the plasma-
15
16 398 impedance signals are normalized before their derivatives are taken (cf. Figure 8b).
17
18 399 Notice that decay of the droplet-induced effect on plasma impedance is similar for H₂O
19
20 400 and D₂O and that it takes a comparatively long time (~10 ms) for the plasma impedance
21
22 401 to return to its steady-state value for both. The similar restoration time for H₂O and D₂O
23
24 402 supports our previous hypothesis [23] that to re-establish the energy-coupling equilibrium,
25
26 403 not only must hydrogen (protium or deuterium) be completely flushed from the system
27
28 404 but also the temperature distribution among plasma species needs to be restored. It is
29
30 405 reasonable that complete flushing and replacement of protium or deuterium takes a
31
32 406 similar length of time. Furthermore, slow thermal diffusion and ambipolar diffusion [51]
33
34 407 constitute the rate-limiting step for temperature redistribution in the ICP. As a result, the
35
36 408 time taken for the plasma impedance to return to its steady-state value is independent of
37
38 409 the isotopic form of hydrogen in the introduced water droplets.
39
40
41
42
43
44
45
46
47
48

49 410 In our previous study [23], we identified four important transitions in the droplet-induced
50
51 411 plasma-impedance change, which were further found to correlate with distinct stages of
52
53 412 plasma perturbation. The four transition points are evidenced by either a change of sign
54
55 413 or slope in the rate of change of the phase-detector signals. The present experiment
56
57 414 revealed one distinctly different condition from our previous report [23]. In that earlier
58
59
60
61
62
63
64
65

1
2
3
4 415 work, the droplet did not undergo complete evaporation in the load-coil region and we
5
6 416 observed localized H atomic and OH molecular emission continuously travelling upward
7
8
9 417 from -15 mm to +1 mm in height (referenced to the top of the load coil) in the captured
10
11 418 monochromatic images [23]. In contrast, in the present study, complete solvent
12
13
14 419 evaporation was accomplished around midway within the load coil region.

15
16
17
18 420 The use of conditions so that droplet vaporization was complete within the load coil
19
20 421 region was intentional here for two reasons. First, if droplet evaporation is not complete,
21
22
23 422 it would be difficult to gauge the relative sizes of the H₂O and D₂O droplets. Only if the
24
25 423 hydrogen emission cloud disappeared and the analyte cloud emerged at the same height
26
27
28 424 for H₂O and D₂O droplets, can one assess the relative sizes of the two aerosols. An
29
30 425 added complication of incomplete evaporation is that it would then be difficult to gauge
31
32
33 426 the relative amount of protium and deuterium released in the load-coil region by the H₂O
34
35 427 and D₂O droplets, respectively. Consequently, it would be difficult to compare the
36
37
38 428 change in plasma impedance and plasma shrinkage induced by H₂O and D₂O droplet
39
40 429 introduction, as it would have been impossible to rule out the possibility of different
41
42 430 amounts of hydrogen being released in the load-coil region. Second, if complete
43
44
45 431 evaporation occurs inside the load-coil region, one can validate the previously observed
46
47
48 432 correlation between transition points and different stages of plasma perturbation and
49
50 433 provide additional experimental basis to revise the correlation, if needed.

51
52
53
54 434 The first transition point (arrow I in Figure 8) occurs when the phase-detector signal
55
56 435 shows its maximum rate of change; this point occurs at the trough of the first derivative
57
58
59 436 because the phase-detector signal moves negative when the plasma is perturbed by an
60
61
62
63
64
65

1
2
3
4 437 aerosol droplet. The first transition points were around 0.63 and 0.73 ms for H₂O and
5
6 438 D₂O droplets, respectively (cf. Figure 8b). The first transition point was previously found
7
8
9 439 [23] to correspond to the moment when the thermal pinch and plasma shrinkage became
10
11 440 established in the load-coil region of the plasma. Figure 7c supports this observation;
12
13
14 441 argon emission clearly drops at the edge of the plasma (i.e., thermal pinch and plasma
15
16 442 shrinkage) at ~0.7 ms. Therefore, the same conclusion applies in the present case in
17
18
19 443 which droplet evaporation is complete within the load coil region.
20
21
22

23 444 The second transition point (arrow II in Figure 8) is defined as the instant when the
24
25 445 induced change in phase-detector signal is at its maximum (i.e., zero derivative), which
26
27 446 occurred at 1.61 and 1.75 ms for H₂O and D₂O droplets, respectively (cf. Figure 8b).
28
29
30 447 This transition point corresponds to the time when the microdroplet was close to the
31
32 448 center of the load-coil region (cf. Figure 4), in excellent agreement with previous findings
33
34
35 449 [23].
36
37
38

39 450 The third transition (arrow III in Figure 8) happens when the rate of change in phase-
40
41 451 detector signal attains its maximum in the direction opposite to that of the first transition,
42
43 452 and before it begins to return to the baseline [23]. For H₂O and D₂O droplets, the third
44
45
46 453 transition arose at ~2.0 and ~2.4 ms, respectively. In our previous work [23], this
47
48
49 454 transition was found to correlate with the time when the droplet moved out of the load-
50
51 455 coil region. Clearly, this interpretation needs to be revised here because the droplets were
52
53
54 456 completely vaporized within the load coil. From Figure 7c, the reduced Ar emission in
55
56 457 the plasma center exhibited sharp recoil from 2.0 to 2.4 ms. Therefore, it is reasonable to
57
58
59
60
61
62
63
64
65

1
2
3
4 458 revise our interpretation of the third transition as the time when the localized cooling
5
6 459 effect of a droplet in the plasma center moves out of the load-coil region.
7
8
9

10 460 The fourth transition (arrow IV in Figure 8) arises when the rate of change in phase-
11
12 461 detector signal begins to asymptotically approach its original, unperturbed level [23]. It
13
14
15 462 was previously reported [23] that plasma shrinkage started to ease near the fourth
16
17
18 463 transition. In the present study, this transition occurred around 4.8 ms for both H₂O and
19
20 464 D₂O droplets. Although no monochromatic image was taken after 4 ms in the present
21
22
23 465 study, the H_α-PMT signal sheds some light on this transition point. Comparing Figures 1
24
25 466 and 8b, one can see that the fourth transition point coincides with the time when the H_α-
26
27
28 467 PMT signal approaches a horizontal line. Although it had not been explicitly pointed out,
29
30 468 a similar correlation between the final transition points of the phase-detector and H_α-
31
32
33 469 PMT signals also existed in our previous work [23]. Therefore, the decay of the H_α-PMT
34
35 470 signals should serve as an effective indicator for recovery of the plasma to its steady-state
36
37
38 471 conditions. This hypothesis is reasonable if one assumes that the plasma shrinkage and
39
40 472 change in impedance are caused by atomic hydrogen present in the plasma.
41
42
43

44 473 **3.6 Repeatability of change in plasma impedance**

45
46
47

48 474 In our experiments, changing between H₂O and D₂O involves removing and re-installing
49
50 475 the monodisperse droplet generator from the base of the plasma torch. As a result, it was
51
52
53 476 always a concern whether an observed change in plasma impedance between H₂O and
54
55 477 D₂O might be an artifact caused by different mounting positions of the droplet generator.
56
57
58 478 This concern arose because the Farnsworth group [17, 19] reported that in their
59
60
61
62
63
64
65

1
2
3
4 479 experience with the MDMI (monodisperse dried microparticulate injector), which can be
5
6 480 viewed as a monodisperse droplet generator coupled to a laminar-flow oven, the
7
8
9 481 measurement results were very sensitive to the positioning of the micropump at the base
10
11 482 of the oven. Specifically, removal and reinsertion of the pump could cause significant
12
13 483 changes in the position of the droplet stream with respect to the plasma [19]. Our present
14
15 484 experimental setup differed from the MDMI work in the way that the droplet dispenser
16
17 485 (micropump) was directly mounted onto the base of the ICP torch and that no oven was
18
19 486 involved. Our arrangement, without an oven, significantly reduces the travel distance for
20
21 487 the droplet, and we did not observe a noteworthy change in signal response when the
22
23 488 micropump was removed and reinstalled on the ICP torch. Nevertheless, an experiment
24
25 489 was performed to evaluate the effect on our results of removing the micropump, changing
26
27 490 the solution from H₂O to D₂O and vice versa, and reinstalling the micropump.
28
29
30
31
32
33
34

35 491 Figures 9a and 9b show the change in RF-probe and phase-detector signals, respectively,
36
37 492 for four sample-switch cycles. Each temporal trace represents the average of 512
38
39 493 individual droplet-introduction events. For each sample (H₂O or D₂O), clear differences
40
41 494 exist in the amplitude of the temporal profiles of plasma impedance, which could result
42
43 495 from either an irreproducibility in the micropump position or a drift in plasma conditions.
44
45 496 For reasons given in the next paragraph, the variation is more likely caused by drift.
46
47 497 Regardless, the key feature in Figures 9a and 9b is that the several traces for either H₂O
48
49 498 or D₂O are more similar to each other than to the traces from the other sample type.
50
51
52 499 Clearly, H₂O droplets induce a larger change in plasma impedance than D₂O.
53
54
55
56
57
58
59
60
61
62
63
64
65

1
2
3
4 500 Two experiments were performed with the sequence of micropump removal, sample
5
6 501 change and micropump re-installation after each measurement; a third experiment did not
7
8
9 502 involve any sample change and micropump removal during the five repetitive
10
11 503 measurements of the plasma impedance signals. Table 1 compiles ratios of the change in
12
13
14 504 RF-probe and phase-detector signals for D₂O to those for H₂O samples. Clearly, D₂O
15
16 505 induces a significantly and consistently smaller change in plasma impedance than H₂O.
17
18
19 506 Specifically, the range is about 0.52 to 0.80, depending on the experimental conditions
20
21 507 and the probing method. The quoted uncertainties in Table 1 represent the standard
22
23 508 deviations obtained through error propagation between the several measurements taken
24
25
26 509 with H₂O and D₂O samples. Because the measurement uncertainties were similar for all
27
28
29 510 three experiments, it is likely that the observed irreproducibility was caused by drift in
30
31 511 the plasma rather than by a change in micropump position during its removal and re-
32
33 512 installation. Further, the three experiments whose results are presented in Table 1 were
34
35
36 513 performed under slightly different conditions so that droplet evaporation was incomplete,
37
38 514 complete near the top of the load coil, or complete midway in the load-coil region.
39
40
41 515 Overall, the ratios are comparable, suggesting that the smaller plasma-impedance change
42
43 516 induced by D₂O droplets than H₂O droplets is a general observation not related to the
44
45
46 517 position of complete droplet evaporation.

518 **3.7 Species responsible for plasma shrinkage and change in plasma impedance**

519 From the foregoing discussion, it is unambiguous that the impact from introduction of
520 H₂O droplets is considerably larger than that from D₂O. Such a difference is not
521 surprising. Plasma shrinkage has been widely reported in situations when a foreign

1
2
3
4 522 substance (e.g., organic solvent [48, 52] or molecular gas [25, 53-55]) is introduced into
5
6 523 the plasma. Because such substances have a higher thermal conductivity than the plasma
7
8
9 524 gas (argon), it is reasonable to link plasma shrinkage and impedance change observed
10
11 525 here to the species that are known to have the highest thermal conductivity: atomic
12
13
14 526 hydrogen [56], from decomposition of water. Conveniently, atomic hydrogen (protium
15
16 527 or deuterium) is monatomic, so the thermal conductivity of the two isotopes can be
17
18
19 528 readily compared since they vary as $\text{mass}^{-1/2}$ [26-28]. This means that thermal
20
21 529 conductivity of atomic deuterium is about 71% of that of atomic protium, which agrees
22
23
24 530 well with the ratios of the change in plasma impedance induced by D₂O to H₂O droplets
25
26 531 (cf. Table 1). Although this correlation is strong, the present experiment provides only
27
28
29 532 indirect support that atomic hydrogen is the species mainly responsible for the strong
30
31 533 thermal pinch and change in plasma impedance. Accordingly, we should consider and
32
33
34 534 eliminate other possibilities as much as possible in order to establish greater confidence
35
36 535 in assigning the role of atomic hydrogen.

37
38
39
40 536 The first possibility to be considered is the thermal conductivity of H₂O and D₂O
41
42 537 molecules. After all, the thermal conductivities of gaseous H₂O and D₂O are also higher
43
44
45 538 than that of argon. For example, the thermal conductivities of gaseous D₂O and Ar at
46
47 539 2500 K are, respectively, 0.31 [57] and 0.08 [58] W m⁻¹ K⁻¹. However, the thermal
48
49
50 540 conductivity ratios of D₂O to H₂O are very close to unity and range only from 0.95 to
51
52 541 1.05, depending on temperature [57, 59]. For polyatomic molecules such as H₂O and
53
54 542 D₂O, thermal conductivity can no longer be approximated by the $\text{mass}^{-1/2}$ relationship
55
56
57 543 as the internal energy-storage modes of the molecule also play an important role [60].
58
59 544 Because the difference in thermal conductivities between H₂O and D₂O is only a few

1
2
3
4 545 percent, it is unlikely that thermal conductivity of the intact molecules would cause a
5
6 546 change in plasma impedance as large as observed.
7
8
9

10 547 Another possible alternative explanation is a difference in the decomposition kinetics of
11
12 548 H₂O and D₂O. If the dissociation kinetics are very different, the dissimilar release rates
13
14
15 549 of atomic H and D into the plasma would make data interpretation difficult. The
16
17
18 550 decomposition kinetics of H₂O and D₂O were studied in an argon environment at a
19
20 551 temperature of 5000 K and no difference was found within experimental error [61].
21
22
23 552 Therefore, it seems that the thermal pinching effect and the large difference in plasma
24
25 553 response to H₂O and D₂O droplet introduction is most confidently attributable to atomic
26
27
28 554 hydrogen released from decomposition of water.
29
30
31

32 555 **4. Conclusion**

33
34
35 556 The introduction of a single micrometer-sized water droplet causes a significant
36
37 557 perturbation in an ICP. By means of the isotope effect, specifically through the
38
39
40 558 introduction of single H₂O and D₂O droplets, the role of hydrogen in plasma
41
42 559 perturbations was clarified. Specific perturbations explored here include local plasma
43
44
45 560 cooling, plasma shrinkage due to thermal pinching, and changes in plasma impedance.
46
47
48

49 561 Several specific conclusions arise from the study. First, based on both theoretical
50
51 562 arguments and experimental inference, H₂O and D₂O droplets produced by a piezo-
52
53
54 563 electric-based on-demand monodisperse droplet generator are very similar in size; the
55
56 564 D₂O droplets might be marginally larger, but definitely are *not* smaller than those of H₂O.
57
58
59 565 Second, a strong isotope effect was experimentally confirmed in governing the extent of
60
61
62
63
64
65

1
2
3
4 566 plasma shrinkage and changes in plasma impedance. In all cases, D₂O droplets induce
5
6 567 significantly less plasma shrinkage and a smaller shift in plasma impedance.
7
8
9 568 Quantitatively, changes in plasma-impedance signals caused by D₂O droplet introduction
10
11 569 ranged from 52% to 80% of those generated by their H₂O counterparts. As the thermal
12
13
14 570 conductivity of deuterium is only about 70% of that for atomic hydrogen (protium),
15
16 571 atomic hydrogen is believed to play an important role in the thermal-pinch effect in the
17
18
19 572 plasma. In marked contrast, no isotope effect was found in the local cooling caused by an
20
21 573 evaporating droplet. Third, decay of the droplet-induced effect on plasma impedance was
22
23
24 574 similar for H₂O and D₂O and it takes a comparatively long time (~10 ms) for the plasma
25
26 575 impedance to return to its steady-state value for both.

27
28
29
30 576 As was reported in our earlier study [23], the droplet-induced change in plasma
31
32 577 impedance correlates qualitatively with four specific stages of plasma perturbation. This
33
34
35 578 correlation was confirmed in the present study even though, here, complete vaporization
36
37 579 of the droplet occurred in the middle of the load coil.

40 41 580 **Acknowledgements**

42
43
44
45 581 This research was supported in part by the US Department of Energy through Grant DE-
46
47 582 FG02-98ER14890 awarded to Indiana University. Work from Lawrence Berkeley
48
49
50 583 National Laboratory (GC) is partly supported by the US Department of Energy, Office of
51
52 584 Defense Nuclear Nonproliferation Research and Development, under contract number
53
54
55 585 DE-AC02-05CH11231 at the LBNL.

56
57
58
59 586

1
2
3
4 587 **References**
5
6
7

- 8 588 1. J.L. Todoli, L. Gras, V. Hernandis, J. Mora, Elemental matrix effects in ICP–AES, J.
9 589 Anal. At. Spectrom. 17 (2002) 142-169.
10
11 590 2. J. van der Mullen, J. Jonkers, Fundamental comparison between non-equilibrium
12 591 aspects of ICP and MIP discharges, Spectrochim. Acta Part B 54 (1999) 1017-1044.
13
14 592 3. M.W. Blades, B.L. Caughlin, Z.H. Walker, L.L. Burton, Excitation, ionization, and
15 593 spectral line emission in inductively coupled plasma, Prog. Anal. Spectrosc. 10 (1987)
16 594 57-109.
17
18 595 4. J.P. Robin, ICP-AES at the beginning of the eighties, Prog. Anal. Atom. Spectrosc. 5
19 596 (1982) 79-110.
20
21 597 5. J.W. Olesik, Fundamental research in ICP-OES and ICP-MS, Anal. Chem. 68 (1996)
22 598 469A-474A.
23
24 599 6. J.M. Mermet, Is it still possible, necessary and beneficial to perform research in ICP
25 600 atomic emission spectrometry?, J. Anal. At. Spectrom. 20 (2005) 11-16.
26
27 601 7. J.W. Olesik, Elemental analysis using ICP-OES and ICP-MS an evaluation and
28 602 assessment of remaining problems, Anal. Chem. 63 (1991) A12-A21.
29
30 603 8. M.D. Montaña, J.W. Olesik, A.G. Barber, K. Challis, J.F. Ranville, Single particle
31 604 ICP-MS: Advances toward routine analysis of nanomaterials, Anal. Bioanal. Chem.
32 605 408 (2016) 5053-5074.
33
34 606 9. D. Mozhayeva, C. Engelhard, A critical review of single particle inductively coupled
35 607 plasma mass spectrometry – A step towards an ideal method for nanomaterial
36 608 characterization, J. Anal. At. Spectrom. (2020) *in press*.
37
38 609 10. G.M. Hieftje, H.V. Malmstadt, A unique system for studying flame spectrometric
39 610 processes, Anal. Chem. 40 (1968) 1860-1867.
40
41 611 11. G.M. Hieftje, H.V. Malmstadt, A new approach to flame spectrometric analysis
42 612 utilizing isolated droplets of sample solution, Anal. Chem. 41 (1969) 1735-1744.
43
44 613 12. J.B. French, B. Etkin, R. Jong, Monodisperse dried microparticulate injector for
45 614 analytical instrumentation, Anal. Chem. 66 (1994) 685-691.
46
47
48
49
50
51
52
53
54
55
56
57
58
59
60
61
62
63
64
65

1
2
3
4
5
6
7
8
9
10
11
12
13
14
15
16
17
18
19
20
21
22
23
24
25
26
27
28
29
30
31
32
33
34
35
36
37
38
39
40
41
42
43
44
45
46
47
48
49
50
51
52
53
54
55
56
57
58
59
60
61
62
63
64
65

615 13. J.W. Olesik, S.E. Hobbs, Monodisperse dried microparticulate injector – a new tool
616 for studying fundamental processes in inductively coupled plasmas, *Anal. Chem.* 66
617 (1994) 3371-3378.

618 14. J.W. Olesik, Investigating fate of individual sample droplets in inductively coupled
619 plasmas, *Appl. Spectrosc.* 51 (1997) A158-A175.

620 15. J.W. Olesik, J.A. Kinzer, G.J. McGowan, Observation of atom and ion clouds
621 produced from single droplets of sample in inductively coupled plasmas by optical
622 emission and laser induced fluorescence imaging, *Appl. Spectrosc.* 51 (1997) 607-
623 616.

624 16. J.W. Olesik, J.A. Kinzer, Measurement of monodisperse droplet desolvation in an
625 inductively coupled plasma using droplet size dependent peaks in Mie scattering
626 intensity, *Spectrochim. Acta Part B* 61 (2006) 696-704.

627 17. A.C. Lazar, P.B. Farnsworth, Characterization of an inductively coupled plasma with
628 xylene solutions introduced as monodisperse aerosols, *Anal. Chem.* 69 (1997) 3921-
629 3929.

630 18. A.C. Lazar, P.B. Farnsworth, Investigation of the analytical performance of an
631 MDMI-ICP-AES system, *Appl. Spectrosc.* 51 (1997) 617-624.

632 19. A.C. Lazar, P.B. Farnsworth, Matrix effect studies in inductively coupled plasma
633 with monodisperse droplets. Part I: Influence of matrix on vertical analyte emission
634 profile, *Appl. Spectrosc.* 53 (1999) 457-464.

635 20. A.C. Lazar, P.B. Farnsworth, Matrix effect studies in inductively coupled plasma
636 with monodisperse droplets. Part II: Influence of matrix on spatially integrated ion
637 density, *Appl. Spectrosc.* 53 (1999) 465-470.

638 21. G.C.Y. Chan, Z.L. Zhu, G.M. Hieftje, Effect of single aerosol droplets on plasma
639 impedance in the inductively coupled plasma, *Spectrochim. Acta Part B* 76 (2012)
640 87-95.

641 22. H. Miyahara, Y. Kaburaki, T. Iwai, A. Okino, Effects of droplet introduction into the
642 ICP sustained by free-running RF-generator on plasma spectroscopic characteristics,
643 *Bunseki Kagaku* 63 (2014) 109-117.

1
2
3
4
5
6
7
8
9
10
11
12
13
14
15
16
17
18
19
20
21
22
23
24
25
26
27
28
29
30
31
32
33
34
35
36
37
38
39
40
41
42
43
44
45
46
47
48
49
50
51
52
53
54
55
56
57
58
59
60
61
62
63
64
65

644 23. G.C.Y. Chan, G.M. Hieftje, Local cooling, plasma reheating and thermal pinching
645 induced by single aerosol droplets injected into an inductively coupled plasma,
646 *Spectrochim. Acta Part B* 121 (2016) 55-66.

647 24. Y.Q. Tang, C. Trassy, Inductively coupled plasma: The role of water in axial
648 excitation temperatures, *Spectrochim. Acta Part B* 41 (1986) 143-150.

649 25. L. Ebdon, P. Goodall, Slurry atomization using hydrogen-modified inductively
650 coupled plasmas, *J. Anal. At. Spectrom.* 7 (1992) 1111-1116.

651 26. A.A. Tarzimanov, Heat conductivity of monatomic gases, *AIAA Journal* 1 (1963)
652 1497-1498.

653 27. S.C. Saxena, Transport properties of gases and gaseous mixtures at high
654 temperatures, *High Temperature Science* 3 (1971) 168-188.

655 28. G.B. Barton, Isotopic effect in gas-chromatographic analysis of argon for trace
656 oxygen, *Anal. Chem.* 52 (1980) 575-575.

657 29. G.C.Y. Chan, Z.L. Zhu, G.M. Hieftje, Operating parameters and observation modes
658 for individual droplet analysis by inductively coupled plasma-atomic emission
659 spectrometry, *Spectrochim. Acta Part B* 76 (2012) 77-86.

660 30. S. Groh, C.C. Garcia, A. Murtazin, V. Horvatic, K. Niemax, Local effects of
661 atomizing analyte droplets on the plasma parameters of the inductively coupled
662 plasma, *Spectrochim. Acta Part B* 64 (2009) 247-254.

663 31. J.W. Olesik, G.M. Hieftje, Optical imaging spectrometers, *Anal. Chem.* 57 (1985)
664 2049-2055.

665 32. N.N. Sesi, D.S. Hanselman, P.J. Galley, J.A. Horner, M. Huang, G.M. Hieftje, An
666 imaging based instrument for fundamental plasma studies, *Spectrochim. Acta Part B*
667 52 (1997) 83-102.

668 33. W.L. Wiese, J.R. Fuhr, Accurate atomic transition probabilities for hydrogen, helium,
669 and lithium, *J. Phys. Chem. Ref. Data* 38 (2009) 565-719.

670 34. M.A. Gigosos, M.A. Gonzalez, V. Cardenoso, Computer simulated Balmer-alpha, -
671 beta and -gamma Stark line profiles for non-equilibrium plasmas diagnostics,
672 *Spectrochim. Acta Part B* 58 (2003) 1489-1504.

- 1
2
3
4 673 35. A.P. Storey, S.J. Ray, V. Hoffmann, M. Voronov, C. Engelhard, W. Buscher, G.M.
5
6 674 Hieftje, Wavelength scanning with a tilting interference filter for glow-discharge
7
8 675 elemental imaging, *Appl. Spectrosc.* 71 (2016) 1280-1288.
9
10 676 36. W.L. Wiese, D.E. Kelleher, V. Helbig, Variations in Balmer-line Stark profiles with
11
12 677 atom-ion reduced mass, *Phys. Rev. A* 11 (1975) 1854-1864.
13
14 678 37. S. Joachim, Effects of ion motion on hydrogen Stark profiles, *Zeitschrift für*
15
16 679 *Naturforschung A* 32 (1977) 1207-1214.
17
18 680 38. E. Horst, Experimental study of Balmer- α Stark broadening, *Zeitschrift für*
19
20 681 *Naturforschung A* 34 (1979) 188-191.
21
22 682 39. A. Sanchez, R.D. Fulton, H.R. Griem, Measurement of the ion dynamic effect on the
23
24 683 H_{α} and D_{α} lines at low electron densities, *Phys. Rev. A* 35 (1987) 2596-2601.
25
26 684 40. M.A. Gigosos, V. Cardeñoso, New plasma diagnosis tables of hydrogen Stark
27
28 685 broadening including ion dynamics, *J. Phys. B: At., Mol. Opt. Phys.* 29 (1996) 4795-
29
30 686 4838.
31
32 687 41. A.H. Harvey, Properties of saturated liquid D_2O , in W.M. Haynes, D.R. Lide, T.J.
33
34 688 Bruno (eds), *CRC handbook of chemistry and physics*, 95th ed., CRC Press, Boca
35
36 689 Raton, FL, USA (2014) pp. 6—10.
37
38 690 42. E.W. Lemmon, Thermophysical properties of water and steam, in W.M. Haynes, D.R.
39
40 691 Lide, T.J. Bruno (eds), *CRC handbook of chemistry and physics*, 95th ed., CRC Press,
41
42 692 Boca Raton, FL, USA (2014) pp. 6—1.
43
44 693 43. G. Jakli, W.A. Van Hook, Vapor pressure of heavy water at 283-363 K, *J. Chem.*
45
46 694 *Eng. Data* 26 (1981) 243-245.
47
48 695 44. W.S. Drisdell, C.D. Cappa, J.D. Smith, R.J. Saykally, R.C. Cohen, Determination of
49
50 696 the evaporation coefficient of D_2O , *Atmos. Chem. Phys.* 8 (2008) 6699-6706.
51
52 697 45. M.R. Webb, G.M. Hieftje, Improved monochromatic imaging spectrometer, *Appl.*
53
54 698 *Spectrosc.* 60 (2006) 57-60.
55
56 699 46. C. Engelhard, S.J. Ray, W. Buscher, V. Hoffmann, G.M. Hieftje, Correcting
57
58 700 distortion in a monochromatic imaging spectrometer for application to elemental
59
60 701 imaging by glow discharge-optical emission spectrometry, *J. Anal. At. Spectrom.* 25
61
62 702 (2010) 1874-1881.
63
64
65

1
2
3
4
5
6
7
8
9
10
11
12
13
14
15
16
17
18
19
20
21
22
23
24
25
26
27
28
29
30
31
32
33
34
35
36
37
38
39
40
41
42
43
44
45
46
47
48
49
50
51
52
53
54
55
56
57
58
59
60
61
62
63
64
65

703 47. R.E. Russo, G.M. Hieftje, An accurate model for sample droplet acceleration in an
704 air-acetylene flame, *Anal. Chim. Acta* 118 (1980) 293-299.

705 48. D.G. Weir, M.W. Blades, Characteristics of an inductively coupled argon plasma
706 operating with organic aerosols. Part 1. Spectral and spatial observations, *J. Anal. At.*
707 *Spectrom.* 9 (1994) 1311-1322.

708 49. H. Lindner, A. Murtazin, S. Groh, K. Niemax, A. Bogaerts, Simulation and
709 experimental studies on plasma temperature, flow velocity, and injector diameter
710 effects for an inductively coupled plasma, *Anal. Chem.* 83 (2011) 9260-9266.

711 50. L. Flamigni, J. Koch, H. Wiltse, R. Brogioli, S. Gschwind, D. Gunther,
712 Visualization, velocimetry, and mass spectrometric analysis of engineered and laser-
713 produced particles passing through inductively coupled plasma sources, *J. Anal. At.*
714 *Spectrom.* 27 (2012) 619-625.

715 51. H. Kafrouni, Study of electron cooling, diffusion and recombination in a decaying
716 argon arc, *Physica B+C* 98 (1979) 100-112.

717 52. D.G.J. Weir, M.W. Blades, The response of the inductively coupled argon plasma to
718 solvent plasma load: Spatially resolved maps of electron density obtained from the
719 intensity of one argon line, *Spectrochim. Acta Part B* 49 (1994) 1231-1250.

720 53. M. Murillo, J.M. Mermet, Improvement of the energy-transfer with added-hydrogen
721 in inductively coupled plasma atomic emission-spectrometry, *Spectrochim. Acta Part*
722 *B* 44 (1989) 359-366.

723 54. E.H. Choot, G. Horlick, Vertical spatial emission profiles in Ar-N₂ mixed gas
724 inductively coupled plasmas, *Spectrochim. Acta Part B* 41 (1986) 889-906.

725 55. N.N. Sesi, A. Mackenzie, K.E. Shanks, P.Y. Yang, G.M. Hieftje, Fundamental
726 studies of mixed gas inductively coupled plasmas, *Spectrochim. Acta Part B* 49
727 (1994) 1259-1282.

728 56. J. Aubreton, M.F. Elchinger, J.M. Vinson, Transport coefficients in water plasma:
729 Part I: Equilibrium plasma, *Plasma Chem. and Plasma Proc.* 29 (2009) 149-171.

730 57. R. Hellmann, E. Bich, Transport properties of dilute D₂O vapour from first principles,
731 *Mol. Phys.* 115 (2017) 1057-1064.

732 58. S.H.P. Chen, S.C. Saxena, Thermal conductivity of argon in the temperature range
733 350 to 2500 K, *Mol. Phys.* 29 (1975) 455-466.

1
2
3
4
5
6
7
8
9
10
11
12
13
14
15
16
17
18
19
20
21
22
23
24
25
26
27
28
29
30
31
32
33
34
35
36
37
38
39
40
41
42
43
44
45
46
47
48
49
50
51
52
53
54
55
56
57
58
59
60
61
62
63
64
65

734 59. R. Hellmann, E. Bich, An improved kinetic theory approach for calculating the
735 thermal conductivity of polyatomic gases, *Mol. Phys.* 113 (2015) 176-183.
736 60. R. Tufeu, P. Bury, Y. Garrabos, B. Le Neindre, Comparison of the thermal
737 conductivities of water and heavy water, *Int. J. Thermophys.* 7 (1986) 663-673.
738 61. K.H. Homann, A. Haas, Kinetics of the homogeneous decomposition of hydrides, in
739 C.H. Bamford, C.F.H. Tipper (eds), *Comprehensive chemical kinetics volume 4*, 1st
740 ed., Elsevier, (1972) pp. 1-45.

741
742
743

1
2
3
4
5
6
7
8
9
10
11
12
13
14
15
16
17
18
19
20
21
22
23
24
25
26
27
28
29
30
31
32
33
34
35
36
37
38
39
40
41
42
43
44
45
46
47
48
49
50
51
52
53
54
55
56
57
58
59
60
61
62
63
64
65

744 Table 1 Ratio of the change in RF-probe and phase-detector signals induced by
745 D₂O droplet introduction to change induced by H₂O droplets. Listed
746 uncertainties obtained through error propagations of the standard
747 derivations of the individual measurements.

	Area [†] of RF-probe signal	Peak height of RF-probe signal	Area [†] of phase- detector signal	Peak height of phase- detector signal
Sample change* between individual measurements; droplet evaporation was incomplete in the load-coil region (conditions very similar to our previous work [23]); temporal profiles are shown in Figures 9a and 9b; <i>n</i> = 4	0.56±0.07	0.52±0.07	0.63±0.12	0.65±0.09
Sample change* between individual measurements; droplet evaporation was likely complete near the top of the load-coil region; <i>n</i> = 4	0.59±0.11	0.58±0.09	0.71±0.09	0.72±0.05
No sample change* between individual measurements; complete droplet evaporation was midway in the load-coil region; temporal profiles are shown in Figure 1; <i>n</i> = 5	0.63±0.15	0.64±0.07	0.80±0.09	0.80±0.06

748 [†]Area is defined as the baseline-corrected integrated signal from 0 ms to end of the
749 captured temporal profile, typically at ~8.5 ms.

750 *‘‘Sample change’’ is defined as the sequence of micropump removal, sample change of
751 H₂O–D₂O, and micropump re-installation.
752

1
2
3
4 **Figure Captions**
5

6
7
8 754 Figure 1 Averaged ($n = 5 \times 1280$) oscilloscope traces of the signals from the H_{α} -
9
10 755 PMT, the RF-probe coil and the phase detector during repetitive H_2O and
11
12 756 D_2O single-droplet introduction into the ICP. The RF-probe and phase-
13
14
15 757 detector signals were measured in ac- and dc-coupling modes, respectively.
16
17
18 758 The error bars represent the standard deviations from the five
19
20 759 measurements. Because the temporal traces contain 2500 data points, for
21
22 760 clarity of the figure, error bars are shown only for every 75 data points.
23
24
25 761 Figure 2 Net monochromatic images (i.e., after subtraction of steady-state plasma
26
27 762 emission) of the ICP load-coil region at $H\ I\ 656.3\ \text{nm}$ for H_2O and $D\ I$
28
29 763 $656.1\ \text{nm}$ for D_2O (as marked), during repetitive introduction of
30
31
32 764 monodisperse microdroplets into the ICP. The vertical and horizontal
33
34
35 765 scales marked on the four edges of the images are in units of millimeters.
36
37 766 Time stamps: (a) 1.55 ms, and (b) 1.65 ms after the H_{α} -PMT trigger.
38
39
40 767 Figure 3 Net monochromatic images (i.e., after subtraction of steady-state plasma
41
42 768 emission) of the ICP load-coil region at $Ba\ II\ 455.4\ \text{nm}$ during repetitive
43
44 769 introduction of monodisperse H_2O and D_2O (as marked) microdroplets
45
46
47 770 into the ICP. The vertical and horizontal scales marked on the four edges
48
49 771 of the images are in units of millimeters. Time stamp: 1.65 ms after the
50
51
52 772 H_{α} -PMT trigger.
53
54
55 773 Figure 4 Vertical positions of the H_2O and D_2O droplets in the ICP as a function of
56
57 774 time. The data are fitted with a quadratic function. The three regions
58
59 775 denoted by dotted lines represent the three selected vertical heights at
60
61
62
63
64
65

1
2
3
4
5
6
7
8
9
10
11
12
13
14
15
16
17
18
19
20
21
22
23
24
25
26
27
28
29
30
31
32
33
34
35
36
37
38
39
40
41
42
43
44
45
46
47
48
49
50
51
52
53
54
55
56
57
58
59
60
61
62
63
64
65

776 which spatio-temporal responses were discussed in detail (see text for
777 discussion). The measurement is limited by the size of the binned ICCD
778 pixels, which contributed an uncertainty of 0.07 mm.

779 Figure 5 Temporal profile of spatially integrated Ba II emission over all vertical
780 locations and between ± 2 mm of the plasma center. The dip at ~ 1.9 ms
781 was caused by obstruction of part of the Ba emission cloud by the load
782 coil.

783 Figure 6 (a) Net absolute, and (b) percentage change in Ar I 696.5 nm emission,
784 relative to steady state, at 1.55 ms after the H_{α} -PMT trigger, caused by
785 repetitive introduction of monodisperse H_2O and D_2O microdroplets into
786 the ICP.

787 Figure 7 Temporal profiles of the relative change in Ar I 696.5 nm emission at the
788 left edge (within 0.8 mm) and center (± 0.9 mm) of the plasma during
789 repetitive introduction of monodisperse H_2O and D_2O microdroplets into
790 the ICP. Vertical heights were (a) -14.3, (b) -8.0, and (c) -1.7 mm with
791 reference to the top of the load coil. Note different vertical scales in plots
792 for center and left edge of plasma.

793 Figure 8 Rates of change (first derivatives) of (a) originally measured, and (b)
794 normalized H_{α} -PMT, RF-probe coil and phase-detector signals during
795 repetitive H_2O and D_2O single-droplet introduction into the ICP. Four
796 notable transitions in the temporal profiles and their derivatives are
797 marked as Arrows I, II, III and IV (see text for discussion). The error bars
798 represent the standard deviations from the five measurements. Because

1
2
3
4
5
6
7
8
9
10
11
12
13
14
15
16
17
18
19
20
21
22
23
24
25
26
27
28
29
30
31
32
33
34
35
36
37
38
39
40
41
42
43
44
45
46
47
48
49
50
51
52
53
54
55
56
57
58
59
60
61
62
63
64
65

799 the temporal traces for the derivatives contain 100 data points, for clarity
800 of the figure, error bars are shown only for every 3 data points.
801 Figure 9 Temporal profiles of (a) RF-probe, and (b) phase-detector signals during
802 repetitive H₂O and D₂O single-droplet introduction into the ICP. Four
803 individual measurement cycles between the H₂O and the D₂O samples
804 were acquired. The sequence of micropump removal, sample change
805 between H₂O and D₂O, and micropump re-installation was performed
806 between trials in each set of measurements.

Figure 1

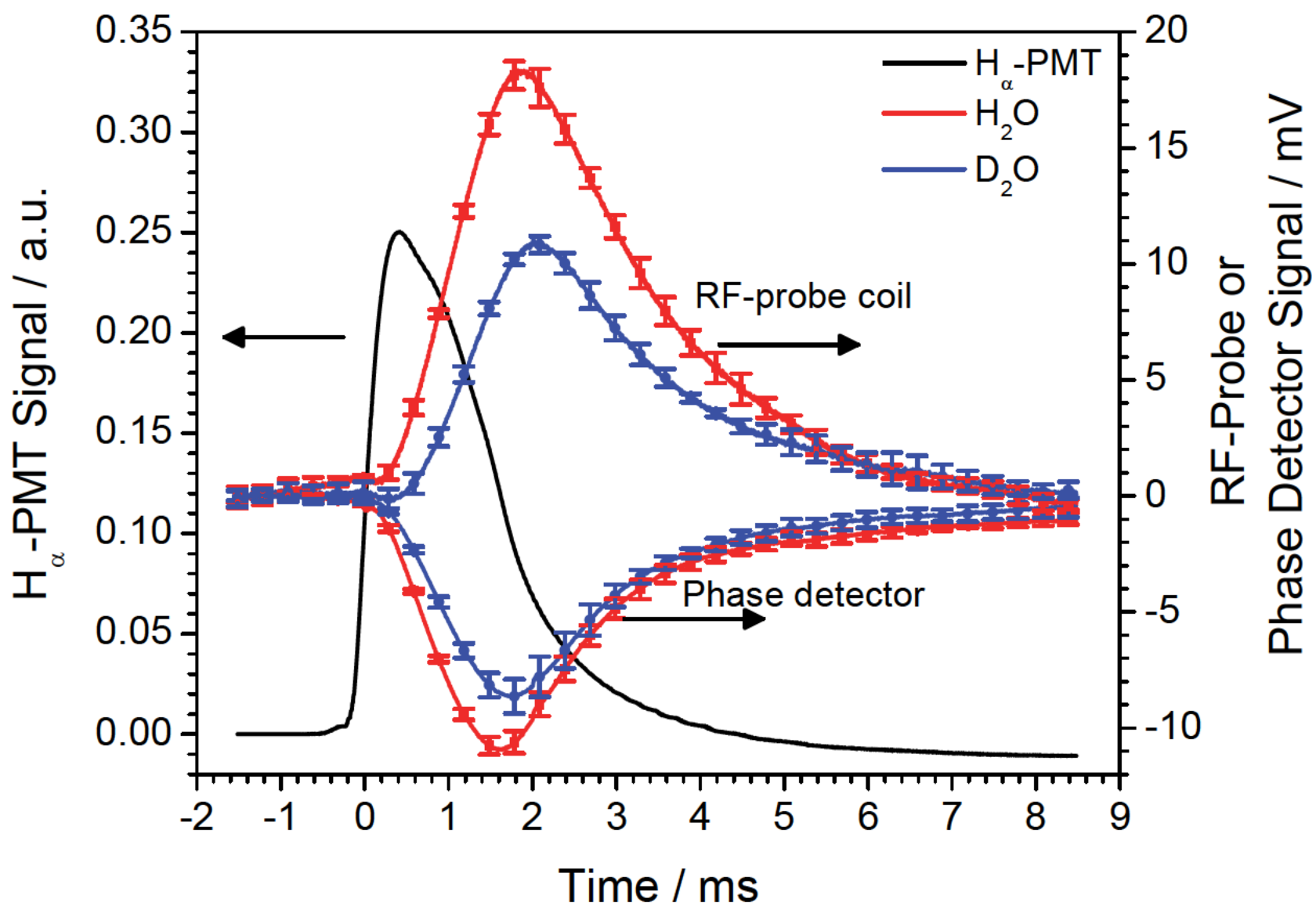


Figure 2a

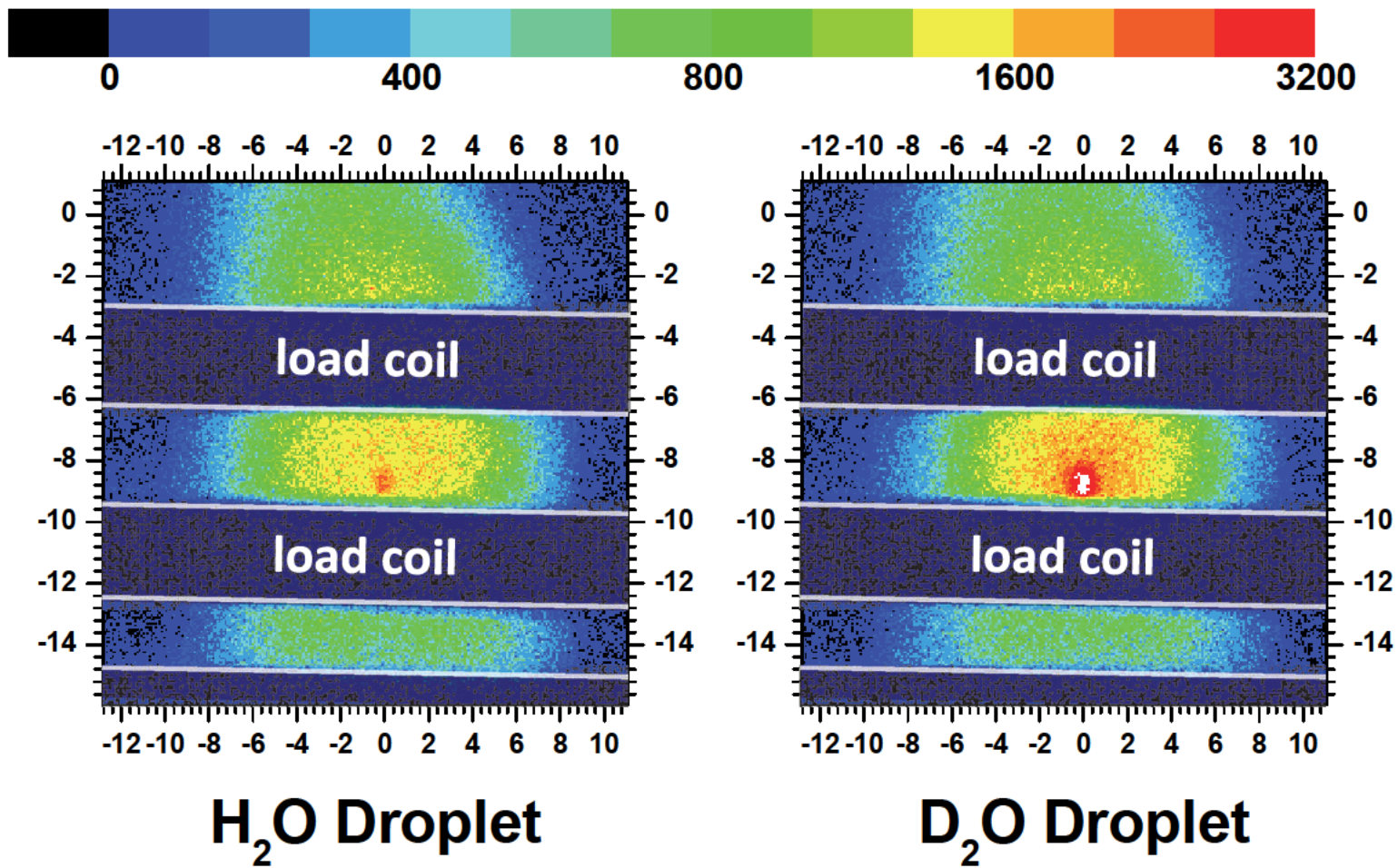


Figure 2b

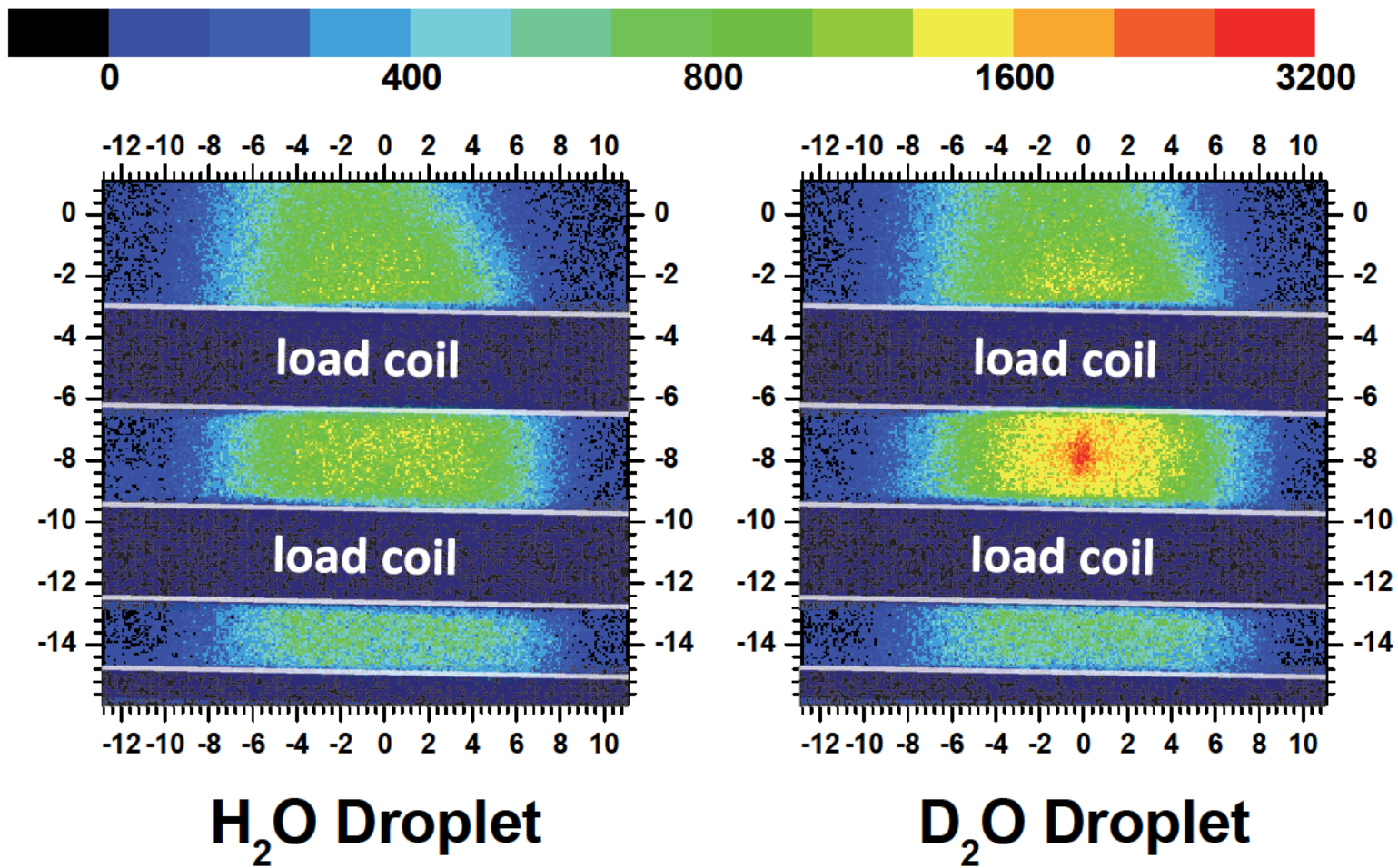


Figure 3

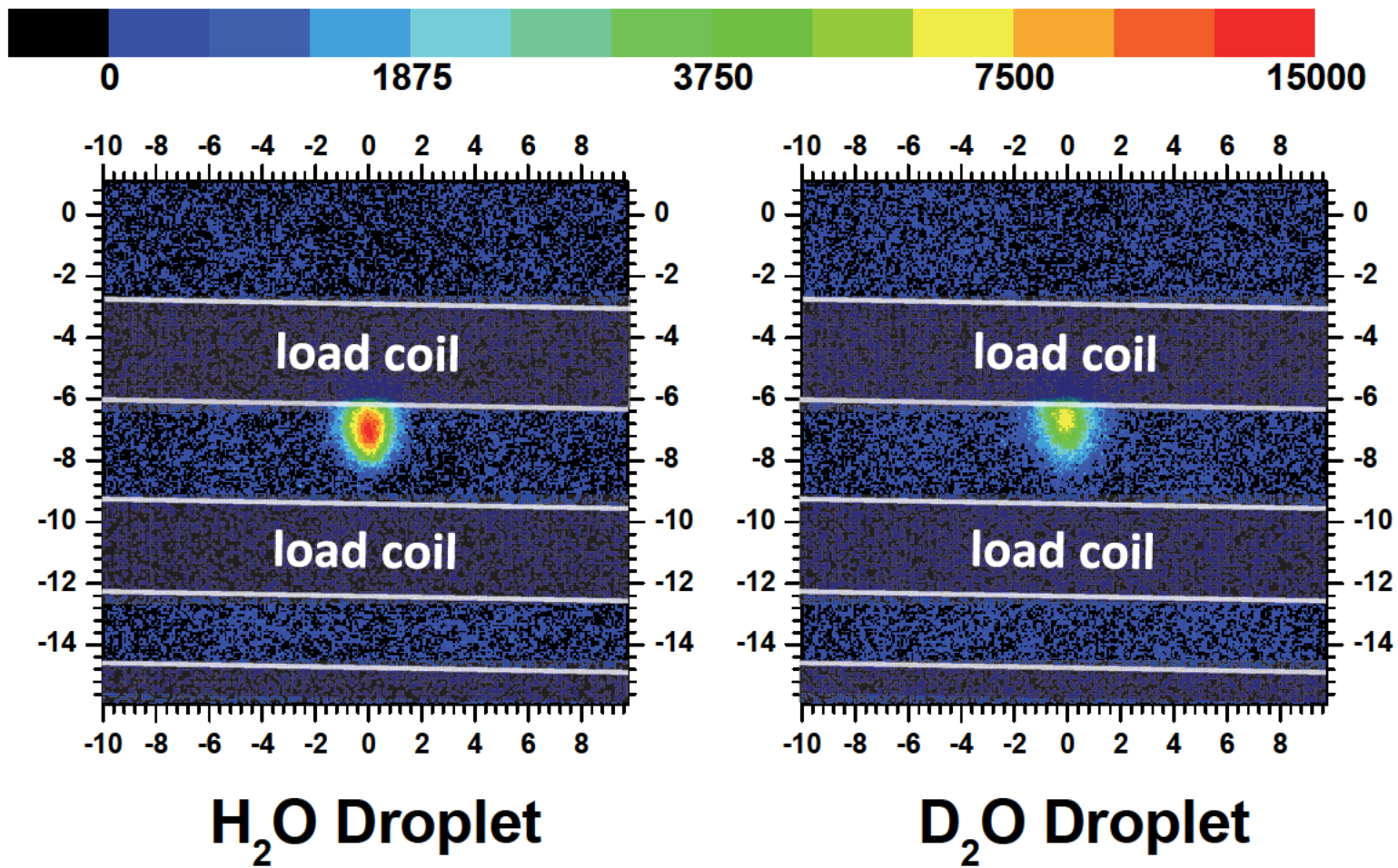


Figure 4

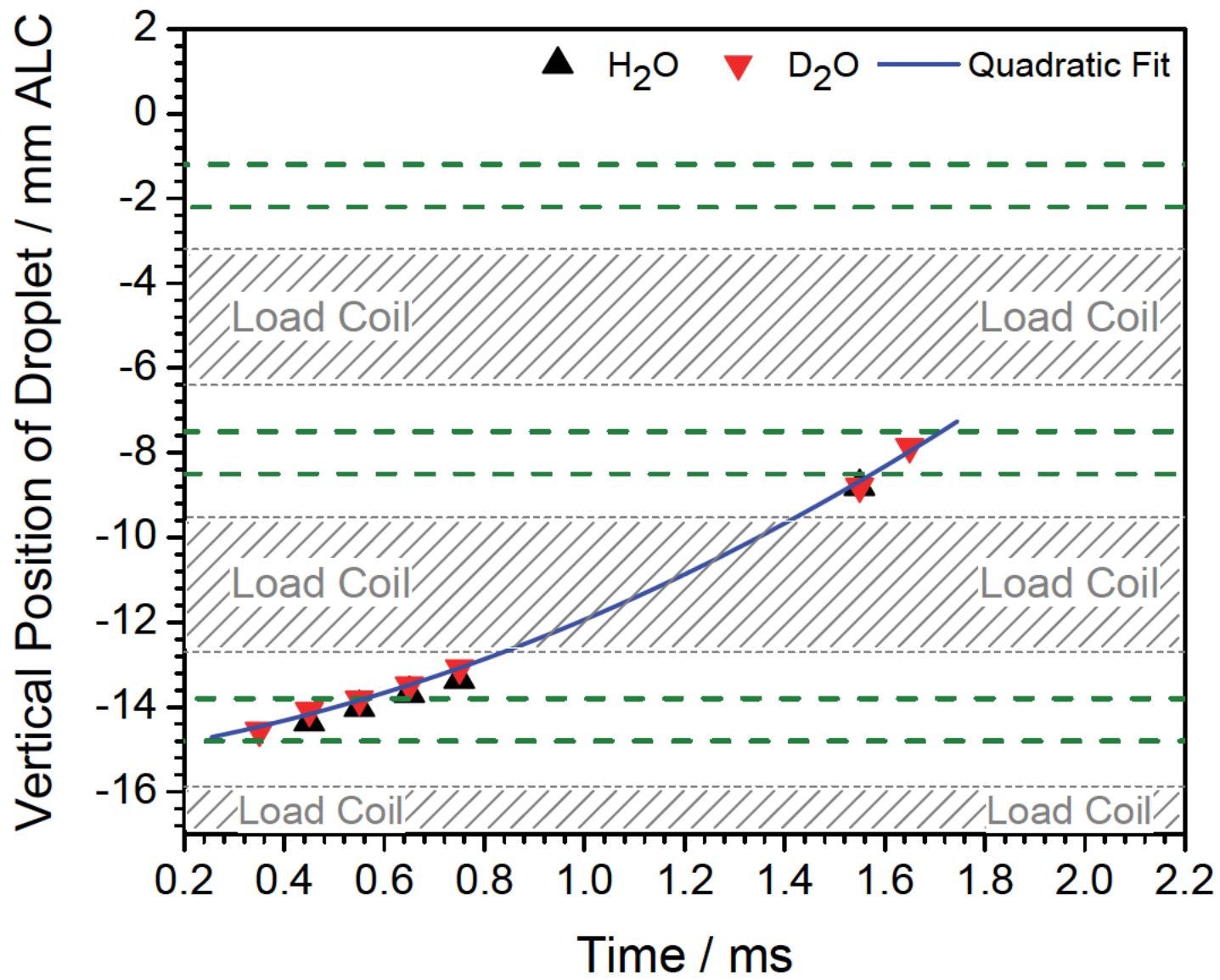


Figure 5

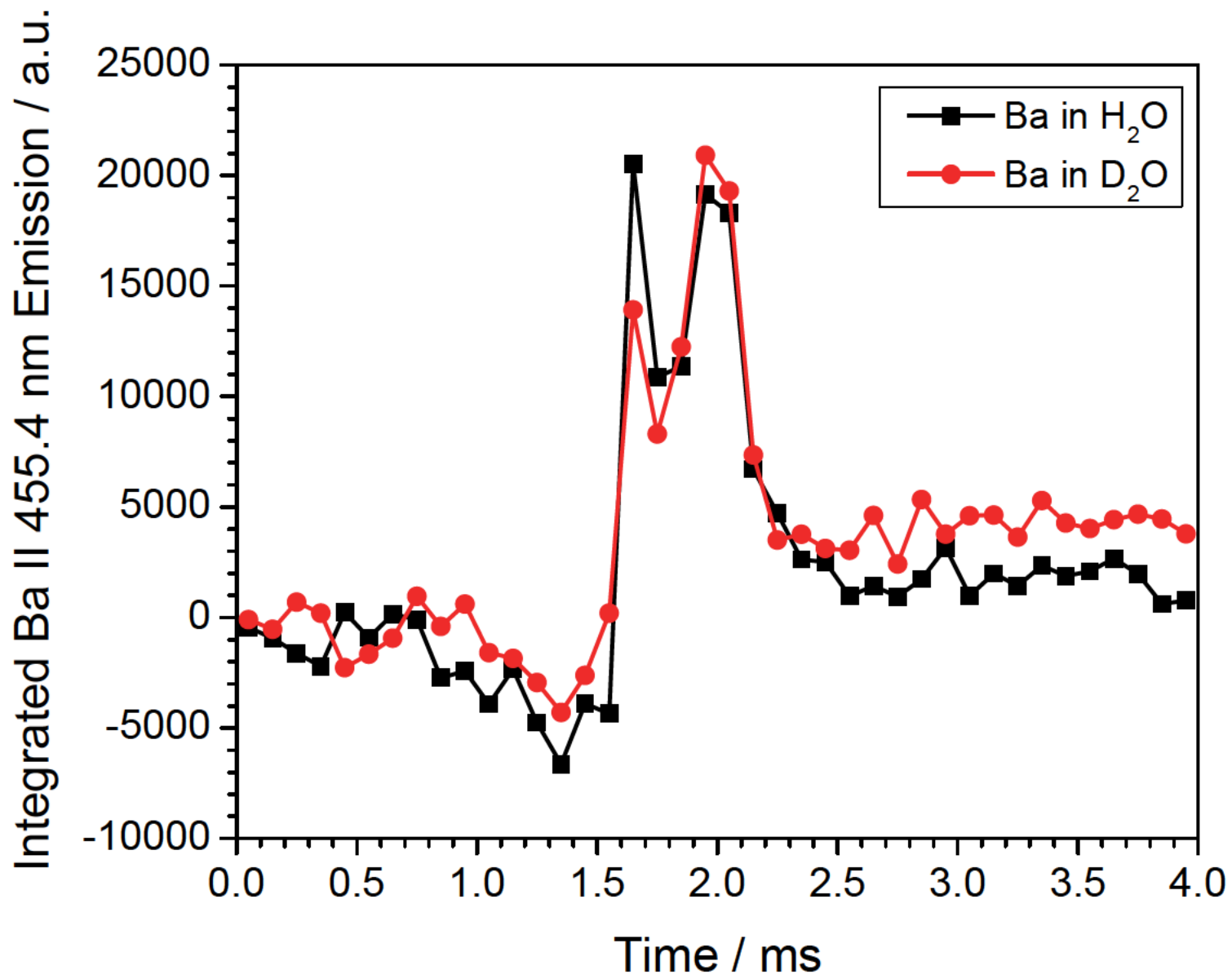


Figure 6a

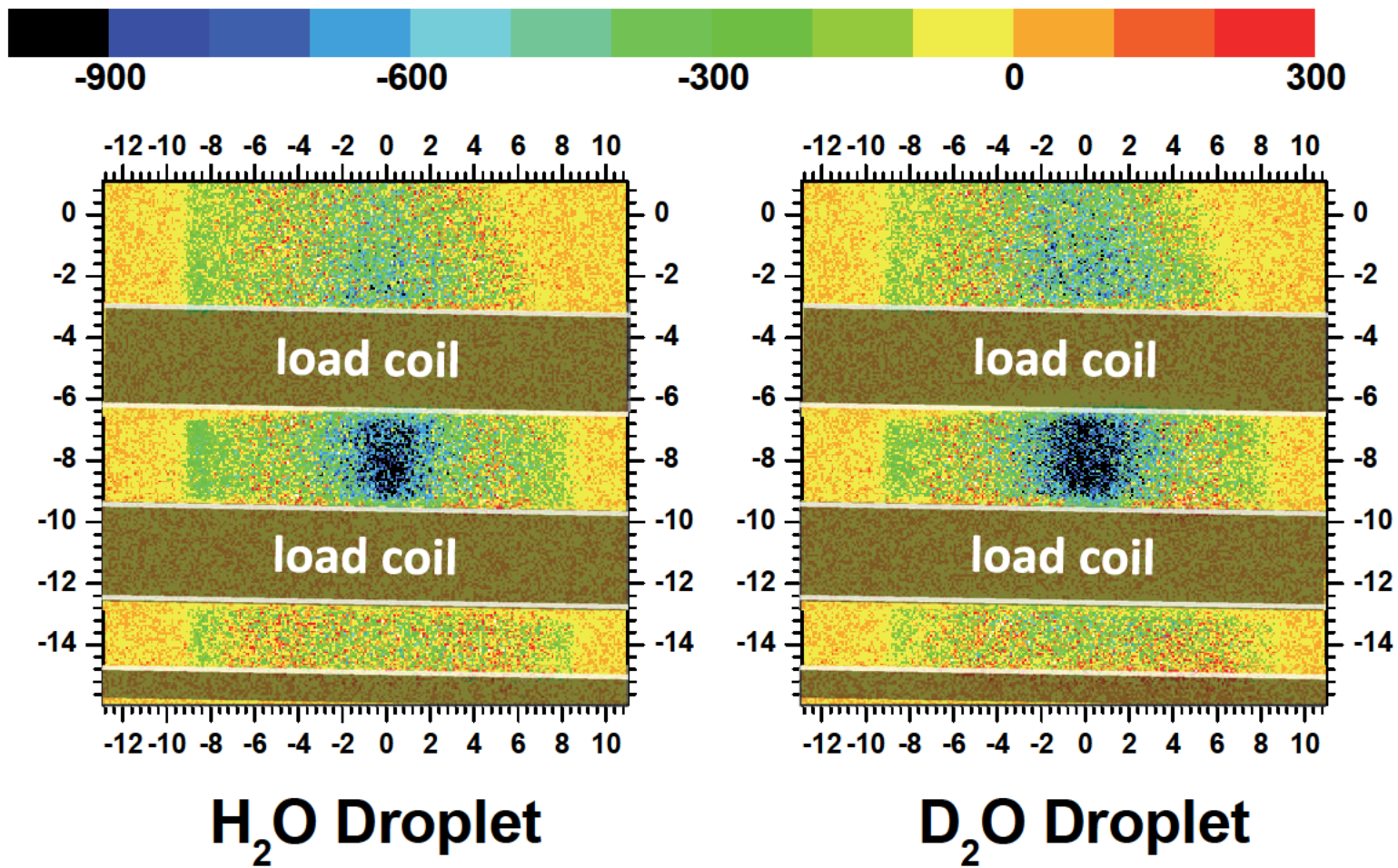


Figure 6b

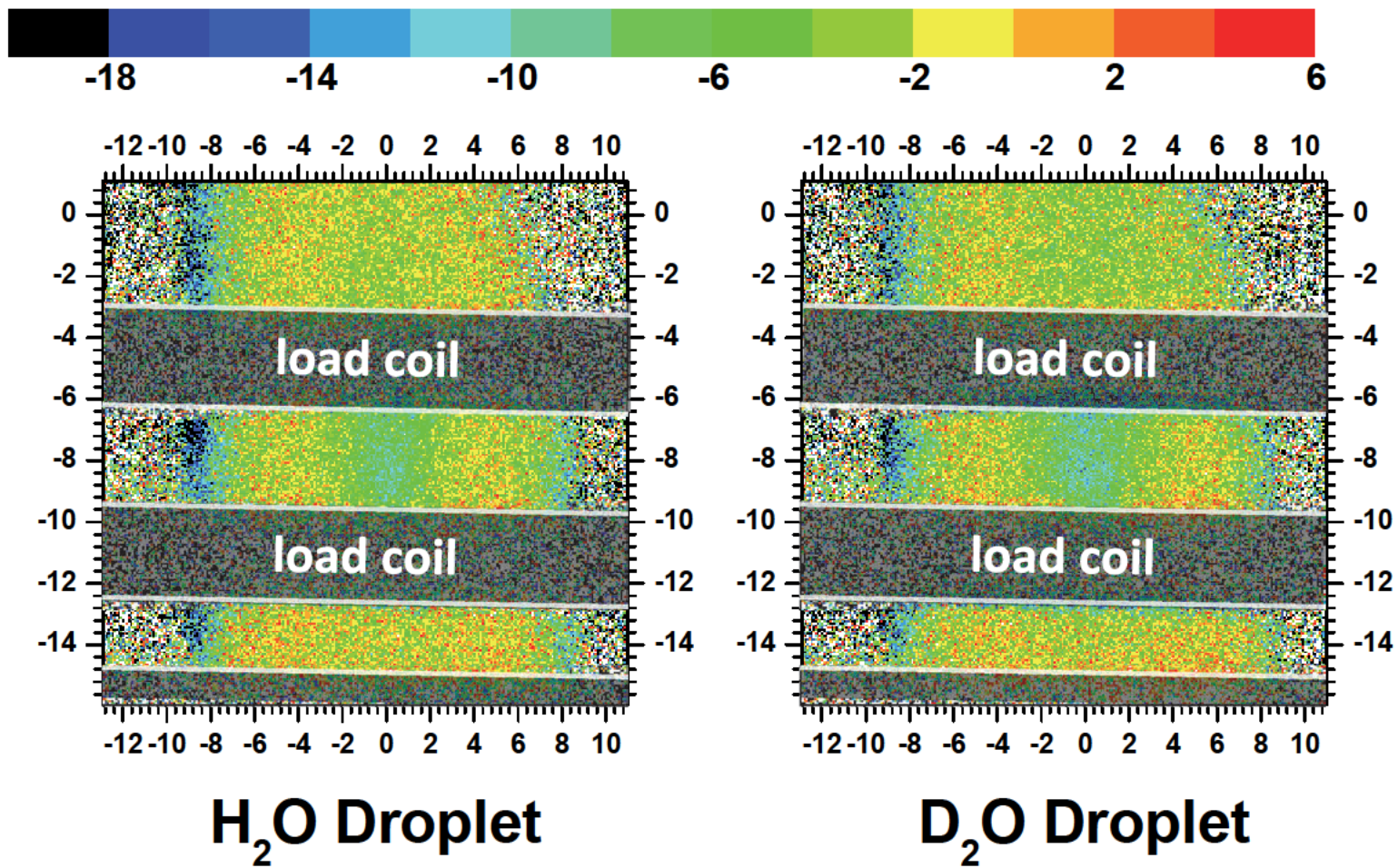


Figure 7a

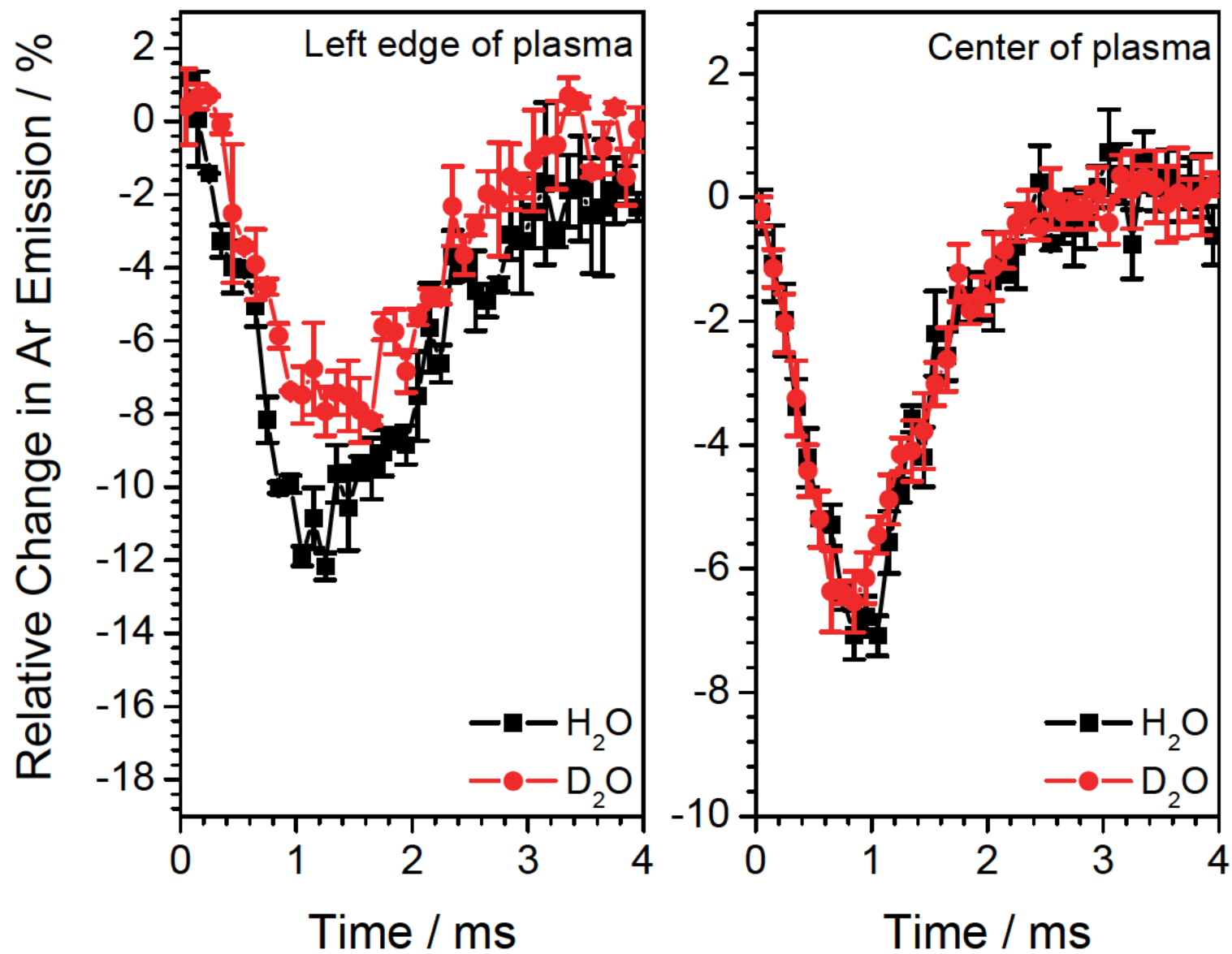


Figure 7b

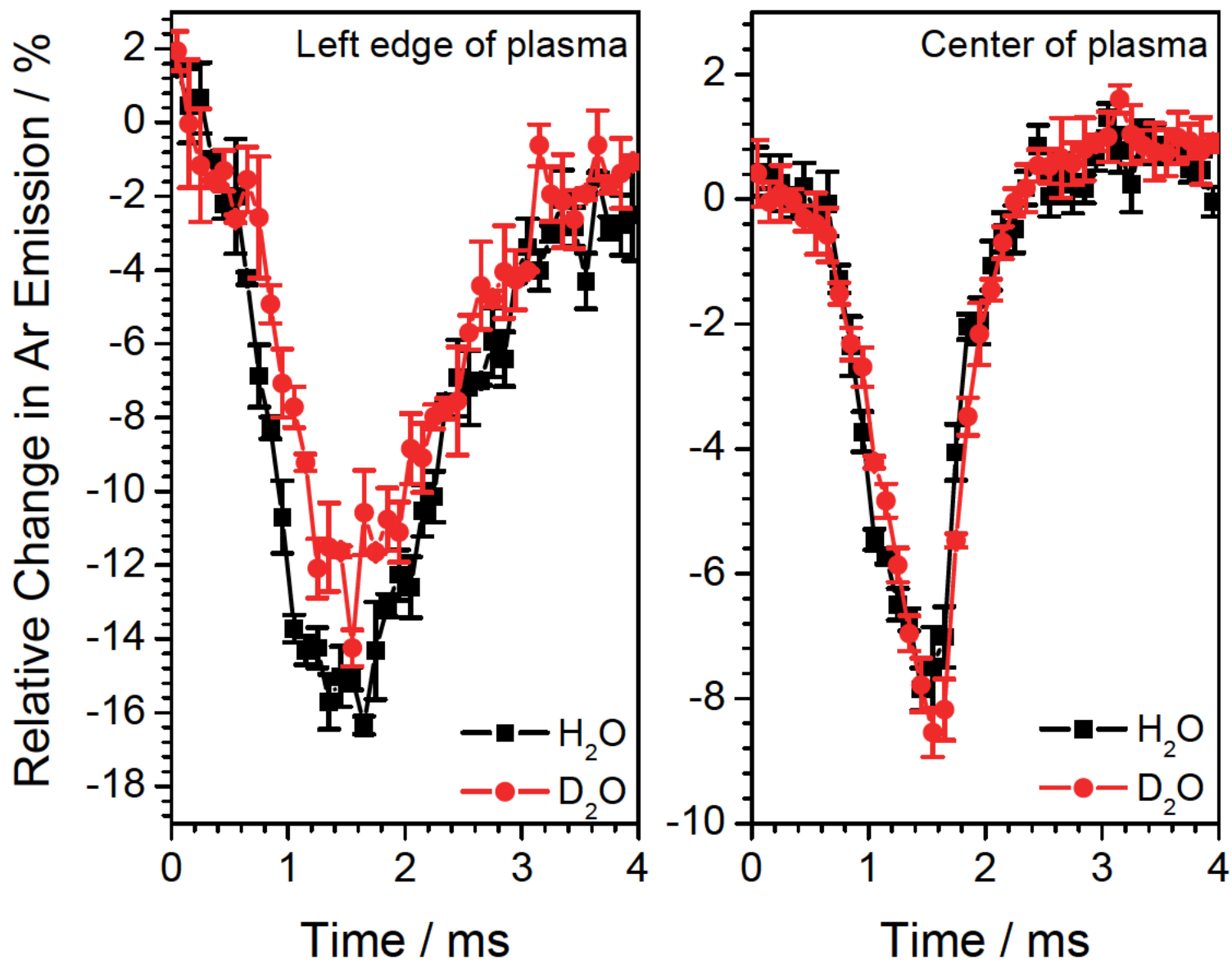


Figure 7c

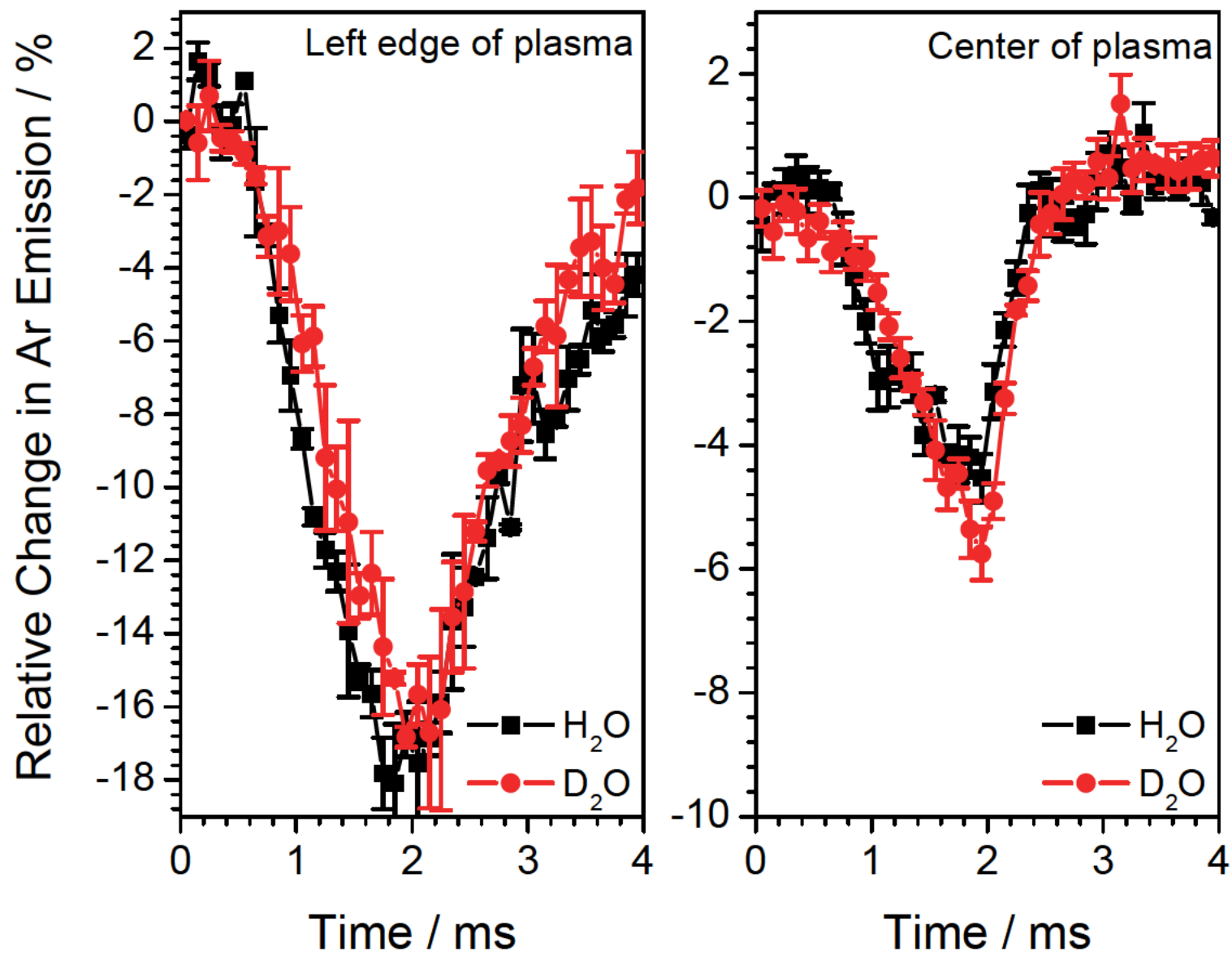


Figure 8a

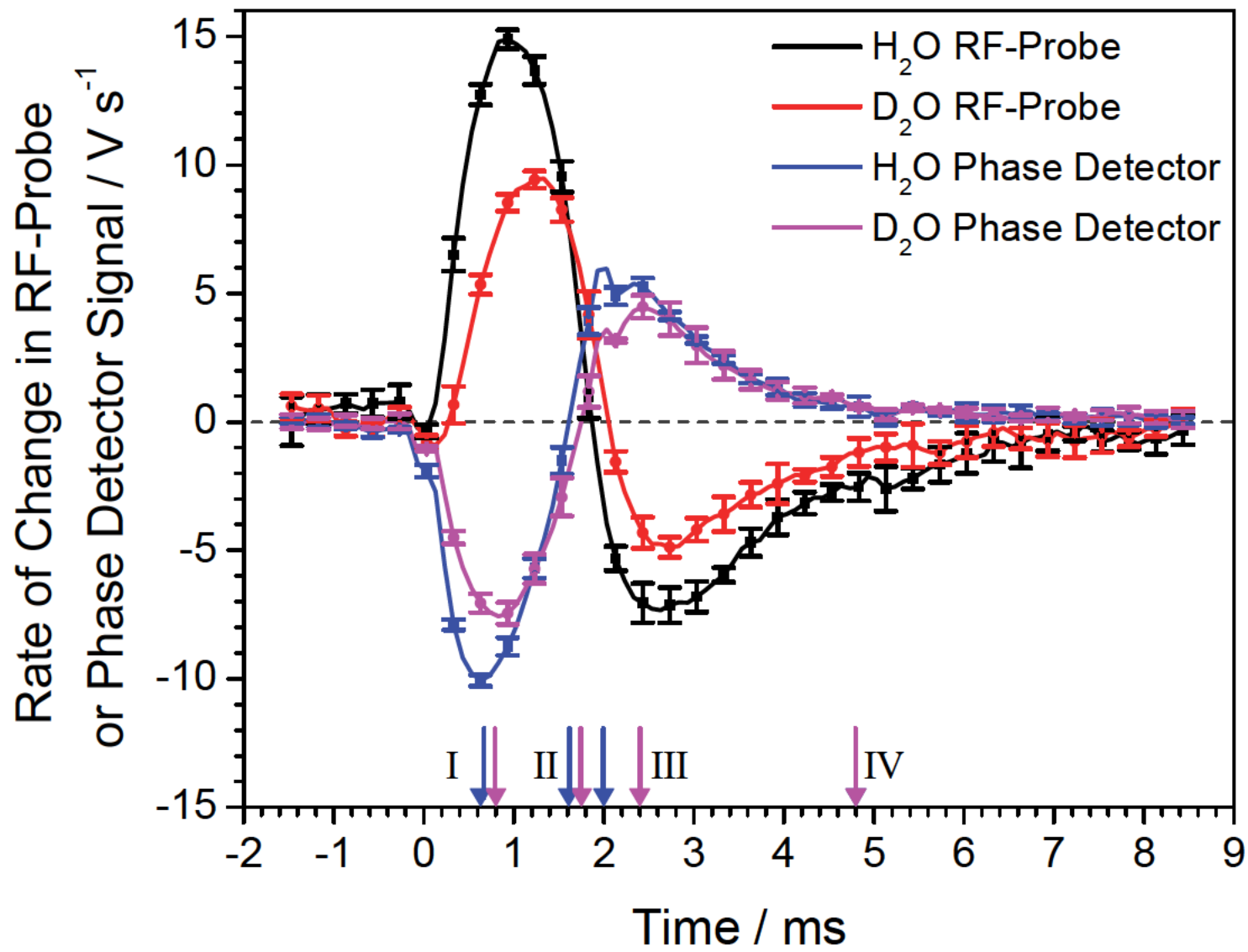


Figure 8b

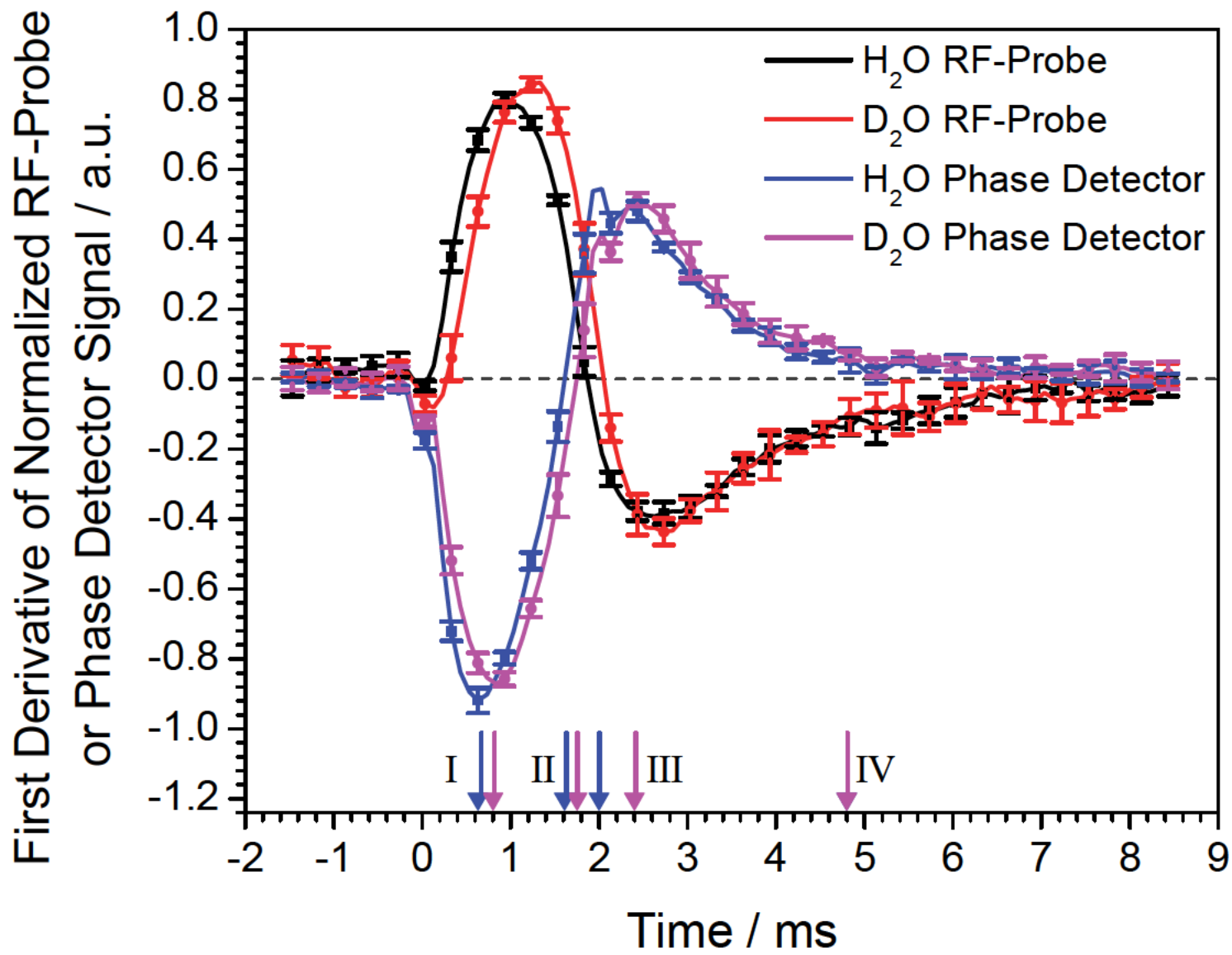


Figure 9a

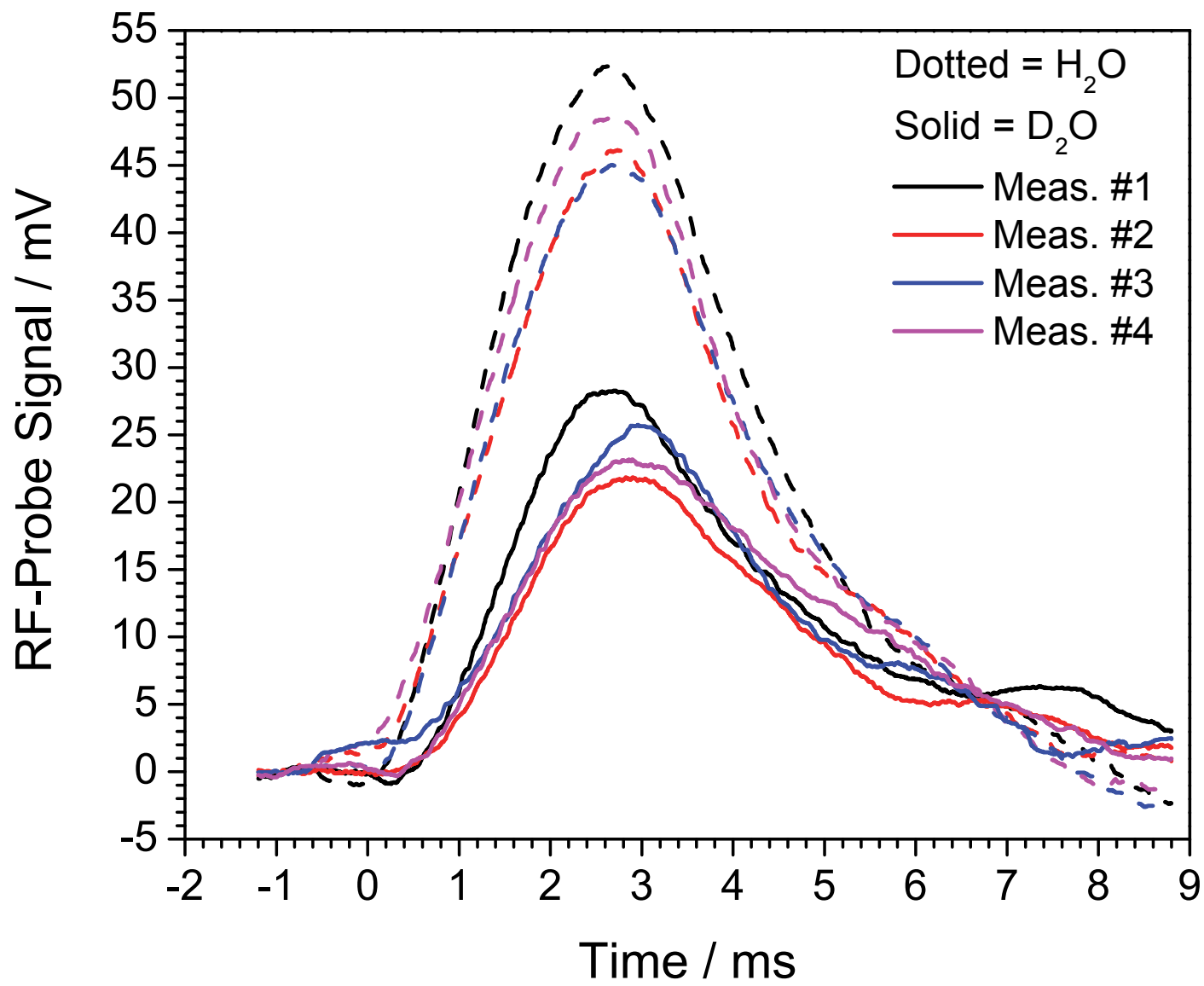


Figure 9b

